POSTER SESSION

Intercalibration of the San Pedro Mártir and CTIO DIMM units

J. Manuel Nuñez,[*] Joaquin Bohigas, Francisco Lazo, David Hiriart,
Tomas Calvario, Osiris Escoboza and Francisco Guillén
Universidad Nacional Autónoma de México, Instituto de Astronomía

ABSTRACT

We compare simultaneous seeing measurements produced by the differential image motion monitor (DIMM) units used at the Observatorio Astronómico Nacional at San Pedro Mártir (SPD) and at Cerro Tololo Inter-American Observatory (RoD), for a total of 14 nights. For the entire data set, made of 1581 nearly-synchronous measurements, we find that the mean and median RoD-SPD seeing differences are +0.004 ± 0.138 and 0.010 in arcsec units respectively.

---

[*] *Corresponding author address:* J.Manuel Nuñez, Instituto de Astronomía, Km. 103 Carretera Tijuana-Ensenada, Ensenada B.C. 22860, México.
E-mail: jnunez@astrosen.unam.mx

1. Introduction

San Pedro Mártir Observatory (SPM)is one of the sites where the Thirty Meter Telescope (TMT) project is conducting its research. To asses how their instrumentation compares with other setups, TMT brought to SPM a RoboDIMM unit (RoD) similar to the one installed at CTIO (Walker et al. 2003).

The presence of this instrument was an opportunity to put in perspective previous seeing measurements made at SPM using a the SPM DIMM unit (SPD). This unit is a replica of the DAC/IAC DIMM described by Vernin and noz Tuñón (1995).

We present the results of simultaneous seeing measurements using SPD and RoD units at SPM during 14 nights in 2005.

2. Instrumental noise of SPD unit

An artificial star was created in order to determine the instrumental noise of the SPD unit. This star was produced with an auxiliary telescope, illuminated at the focal plane by a 125 μm diameter optical fiber in contact to a LED operating at λ = 660 nm (see Figure 1). The setup produces 2 fixes spots from where the centroids were measured. The random noise of the SPD it is 0.032 arcsec.

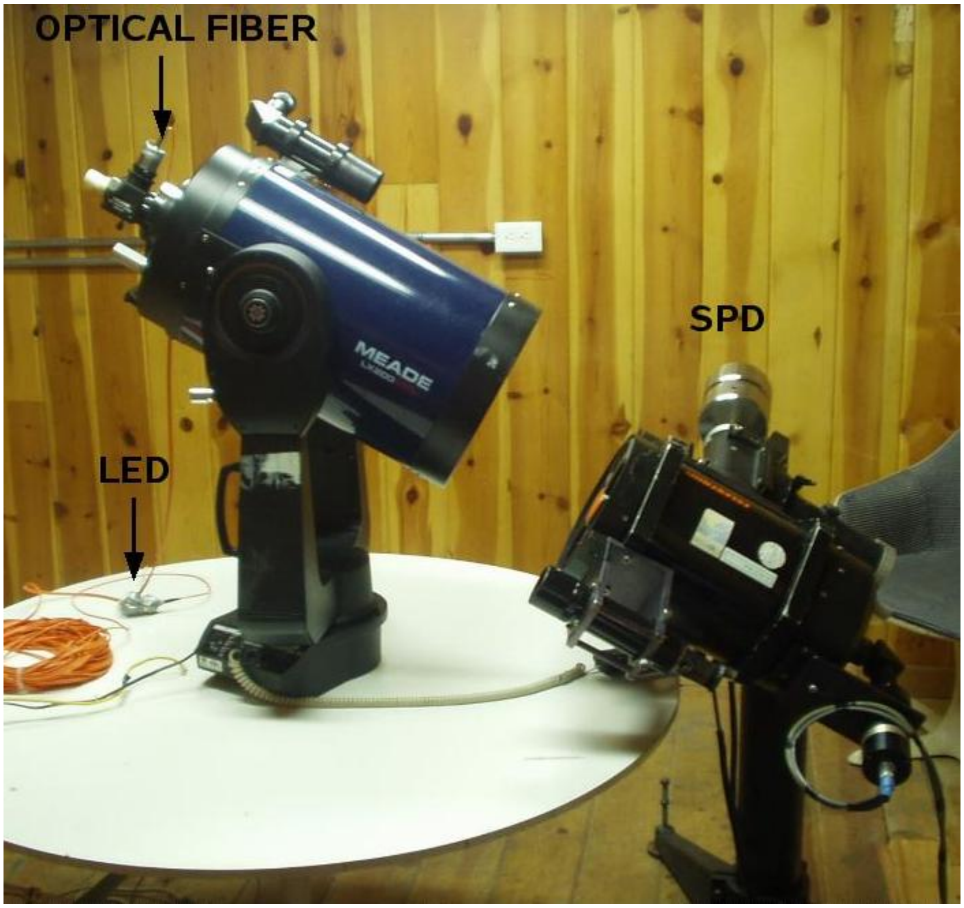

FIG. 1. Setup to determine the instrumental noise of SPD.

3. SPD and RoD units

Some technical parameters of SPD and RoD are listed in Table 1. A more complete description of SPD can be found in Vernin and noz Tuñón (1995), noz Tuñón et al. (1997) and Michel et al. (2003a,b). The RoD is described in Walker et al. (2003), Bustos et al. (2004) and www.ctio.noao.edu/telescopes/dimm/dimm.html.

4. Comparison between SPD and RoD

Simultaneous seeing measurements from SPD and RoD were carried out during 14 nights. The systems were placed less than 3 meters apart and 1 meter above ground level (a concrete base) in a wind protected area. Thus, operating conditions were virtually identical. Both instruments observed the same stars at all times. These stars were η Uma ($V = 1.86$), β Dra ($V = 2.79$), α Cep ($V = 2.44$) and δ Cas ($V = 2.68$). In the case of SPD, we used a 40×40 pixel window and measurements were accepted only when the difference between the parallel and perpendicular FWHM was not larger than 12% (noz Tuñón et al. 1997). In the case of RoD, measurements were accepted only when the Strehl ratio was larger than 0.5 in both images (Tokovinin 2004). Under these circumstances, the combined instrumental error is 0.044 arcsec (0.032 for SPD and 0.030 for RoD in arcsec units).

In Figure 2 we plot all RoD vs SPD nearly-synchronous seeing measurements, along with a

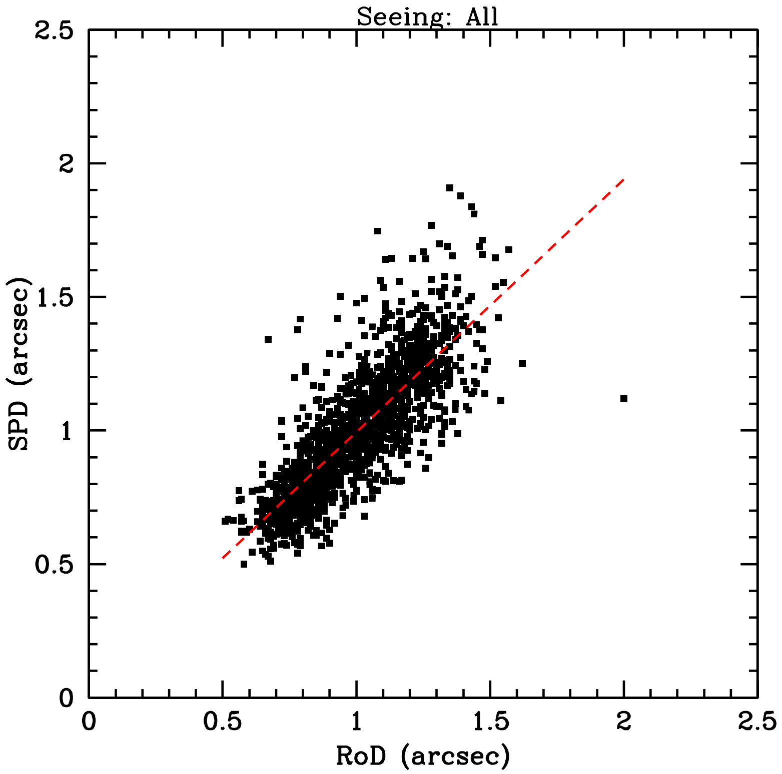

FIG. 2. RoD *vs.* SPD simultaneous seeing measurements. The dotted line is the linear regression to the 1581 data points .

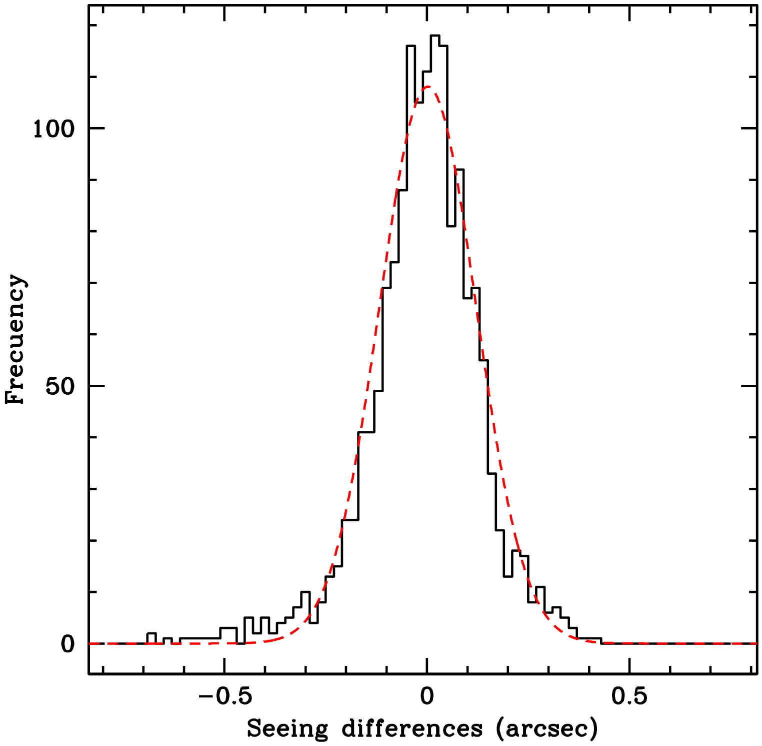

FIG. 3. Histogram for seeing difference RoD-SPD. Data binning is 0.02 arcsec. The dashed line represents the best Gaussian fit to the data.

linear regression to the 1581 data points. The formula for this regression is

$$SPD = 0.95\ RoD + 0.05\ . \tag{1}$$

The correlation coefficient is 0.81. This regression also shows that SPD delivers a smaller mean seeing value than RoD. We analyzed point-to-point differences in three seeing bands as given by SPD: seeing less than 1, between 1 and 1.5 and larger than 1.5 arcsec. Results presented in Table 2 show that RoD tends to deliver a smaller value than SPD as seeing gets worse. The transition between the two smaller seeing bands is small.

In Figure 3 we plot a histogram for the RoD-SPD seeing differences, with binning of 0.02 arcsec. In this figure we also include a Gaussian fit (centered at +0.002 arcsec, with a variance equal to 0.119 arcsec) to all data points.

5. Conclusions

Seeing measurements from SPD and RoD units were compared for 14 nights between the months of June and August, 2005.

For the data set, consisting of 1581 nearly-synchronous measurements, we find that the mean and median RoD-SPD seeing differences are +0.004 ± 0.138 and +0.019 arcsec respectively . An histogram of the RoD-SPD seeing differences can be represented with an excellent Gaussian fit centered at +0.002 arcsec, with a variance equal to 0.119 arcsec.

Acknowledgments.

This work was made possible thanks to the collaboration of the TMT site testing group and the continuous help and advice of those responsible for site testing at CTIO, Edison Bustos in particular. The support of the administrative and technical staff at SPM, in particular Antolín Córdova, is also gratefully acknowledged. Valuable observations made by Mauricio Tapia lead to many improvements in the paper.

TABLE 1. SPD and RoD technical parameters

	SPD	RoD
Telescope	Celestron $8''$	Meade $10''$
Pupil diameter	60 mm	95 mm
Pupil separation	140 mm	150mm
Prism deviation angle	30”	75”
CCD format	576x550 pix	320x240pix
Pixel size	23x23 μm	10x10 μm
Plate scale	$0.6''$/pix	$0.769''$/pix
Intensified	Yes	No

TABLE 2. Near-synchronous RoD-SPD seeing differences in three SPD seeing bands

Seeing band	Number of Points	Δ Avg(arcsec)	ΔMed(arcsec)
All	1581	0.004±0.138	0.010
≤ 1	854	+0.048±0.101	0.041
1 - 1.5	690	-0.032±0.144	-0.033
≥ 1.5	37	-0.310±0.167	-0.292

References

Bustos, E., A. A. Tokovinin, and H. Schwarz, 2004: Ctio manual del robodimm. Tech. Rep. 2.8.

Michel, R., J. Echevarría, R. Costero, and O. Harris, 2003a: *RevMexAA(SC)*, **17**, 93.

Michel, R., J. Echevarría, R. Costero, O. Harris, J. Magallón, and K. Escalante, 2003b: *RevMexAA(SC)*, **39**, 291.

noz Tuñón, C. M., J. Vernin, and A. M. Varela, 1997: *A&AS*, **125**, 183.

Tokovinin, A. A., 2004: Internal report, ctio. Tech. rep., CTIO.

Vernin, J. and C. M. noz Tuñón, 1995: *PASP*, **107**, 265.

Walker, A. R., R. D. Blum, M. Boccas, E. Bustos, H. E. Schwarz, N. Suntzeff, and A. A. Tokovinin, 2003: Proc. SPIE, Vol. 4840, 509.

On the use of Satellite data for Atmospheric Extinction Studies

Antonia M. Varela*
Instituto de Astrofísica de Canarias, Tenerife, Spain

Chiara Bertolin
Institute of Atmospheric and Climate Sciences, Bologna. Italy

Casiana Muñoz-Tuñón, Jesús Jiménez-Fuensalida
Instituto de Astrofísica de Canarias, Tenerife, Spain

Sergio Ortolani
University of Padova, Padova. Italy

ABSTRACT

Atmospheric extinction is the astronomical parameter that evaluates the sky transparency and it is associated with the absorption/scattering of Earth's atmosphere. Sources of sky transparency degradation are the presence of clouds (water vapour) and airborne aerosols (dust particles included). The aerosol index provided by the TOMS (Total Ozone Mapping Spectrometer) is one of the most widely accepted products to detect the daily aerosol content. There are local measurements, since 1984, providing extinction values in routine mode at the Roque de los Muchachos Observatory (ORM-2396m) on La Palma (Canary Islands). Previous works have demonstrated that there is no linear correlation between aerosol index provided by the TOMS and the measured atmospheric extinction coefficient. The reasons behind are the spatial grid sampling of the satellite combined with the abrupt orography of the area. Given that, this situation can also affects to places like Mauna Kea or other sites with similar geographical conditions. We are exploring the usefulness of data provided by different spectrographs onboard NASA and ESA satellites with better spatial and temporal resolutions than TOMS and centered on channels of astronomical interest as a possible tool for site characterization. Data analysis need to be complemented with those provided by in situ instruments (telescopes, airborne particles counters, ground meteorological stations, etc.).

---

*Corresponding author address:Antonia M. Varela, Instituto de Astrofísica de Canarias, C./Via Láctea, S/N, 38200-La Laguna, Tenerife, Canary Islands, Spain
E-mail: avp@iac.es

Some conclusions

The sky transparency is a relevant parameter for astronomical site characterization. This parameter is conceptually related to the aerosol optical thickness and also could be related to the aerosol index obtained with different methods: in situ and remote sensing. Among remote sensing techniques, satellite data measuring aerosols has been recently proposed as a useful technique for site characterization and for searching new sites for hosting future extremely large telescopes. Nevertheless these data need to be critically considered and interpreted in accordance with the spatial resolution and spectroscopic channels used. In situ data are still a necessary reference for calibrating and interpreting the aerosol index provided by different spectrometers aboard satellites.

1. African dust intrusions affect the western and eastern Canary Islands in different ways. The reasons are differences in latitude (distance to the African coast) and sharp orographical contours . The presence of a stable inversion layer and the high peaks of the western islands (Tenerife and La Palma) produces mass flux patterns in the low (mixing) layers, closer to the sea, different from those at the median-upper (or free) troposphere layer.

2. We have compared measurements provided by the TOMS satellite (aerosol index, AI) with other measurements taken at the ORM (2400m above the sea level) with a telescope (CAMC) dedicated to the measurement of atmospheric extinction (KV): there is not linear correlation between both parameters, and this correlation only improves under dust storms episodes, more frequent in summer, when the dust can reach the level of the Observatory. The reasons for such lack of correlation are:

    2.1 The TOMS has a resolution of 1ºx1º, so the AI is averaged over areas whose size covers the entire island of La Palma or Tenerife.

    2.2 The TOMS uses channels centred on the UV to measure AI, and the measurements could be particularly contaminated by the presence of highly reflective clouds. Moreover, AI incorporates absorbent particles in ranges that do not affect atmospheric transparency in the visible range.

4 For this reason the TOMS/Earth Probe is not a useful tool for the characterization of the presence of dust above the Canarian Astronomical Observatories (2400 m above mean sea level), Varela et al. (2004a, 2004b)

5 We have explored the use of other detectors on board different NASA and ESA satellites that operate in bands of astronomical interest (the visible and NIR) and with higher spatial resolution (1km x 1km or better). More details in Varela et. al, (2007).

6 These data must always be compared with local measurements based on air particle detectors (size and density) whose measurements determine the effect of such particles on atmospheric transparency (or extinction): from LIDAR data (INTA) of 30m resolution (NASA MPL-NET-AERONET), by using the IAC

airborne particle counter (from Pacific Scientific Instruments) installed at the ORM in February 2007 (with 6 channels: 0.3, 0.5, 1, 3, 5, 10microns) and by the INM Multi-Filter Rotating Shadow band Radiometer (MFRSR) programmed to be installed at the ORM in summer 2007 (consisting on 6 narrow bands between 414nm and 936nm) that will provide the size, density and vertical distribution of the aerosols.

Acknowledgments.

We express our deepest thanks to the Ozone Processing Team (OPT) of TOMS (NASA) for Aerosol Index calculation and to the Carlsberg Meridian Telescope (CAMC) of the Isaac Newton Group on La Palma for the coefficient extinction data and in both cases for free internet publication. This study is part of the site characterization work developed by the Sky Quality Group of the IAC and has been carried out under the framework of the European Project OPTICON and under the FP6 Proposal for Site Selection for the European ELT.

References

Varela, A.M., J.J. Fuensalida, C. Muñoz-Tuñón, J.M. Rodríguez Espinosa, B. García-Lorenzo and E. Cuevas 2004a: Proc of SPIE Vol. 5571, 105

Varela, A.M., J.J. Fuensalida, C. Muñoz-Tuñón, J.M. Rodríguez Espinosa, B. García-Lorenzo and E. Cuevas 2004b: Proc of SPIE Vol. 5489, 245

Varela, A.M., C. Bertolin, C. Muñoz-Tuñón, J. J. Fuensalida and S. Ortolani, 2007: MNRAS (in preparation)

Dome seeing subtraction from G-SCIDAR measurements

Jesús J. Fuensalida, Begoña García-Lorenzo* and Claudia Hoegemann
Instituto de Astrofísica de Canarias, Tenerife, Spain

ABSTRACT

We have developed an algorithm to eliminate the dome seeing contribution to turbulence profiles derived from G-SCIDAR data. The algorithm, based on the parity of functions, is completely automated and it takes only a few seconds to process a full night of G-SCIDAR data. Seeing measurements obtained from turbulence profiles derived from G-SCIDAR observations and removing the dome contribution with our algorithm are in good agreement with seeing data obtained using Differential Image Motion Monitors (DIMMs). An important advantage of the proposed procedure is that it permits an automated reduction during the calculation process and it could be implemented to work in real time. The formulation to identify the shape of the dome seeing could be extended to other problems of shape recognition whenever it is even.

***Corresponding author address:* Begoña García-Lorenzo Instituto de Astrofísica de Canarias, C/ Via Lactea S/N, 38200-La Laguna, Tenerife, Spain.
E-mail: bgarcia@iac.es

1. Introduction

SCIntillaton Detection and Ranging (SCIDAR hereafter) is a remote sensing technique to measure the strength and velocity of atmospheric turbulence layers. This technique has been extensively explained in several papers (Johnston et al. 2002; Kluckers et al. 1998; Funchs, Tallon & Vernin 1994; Rocca, Roddier & vernin 1974; Vernin & Roddier 1973). The implemation of this technique requires telescopes larger than 80 cm. As a consequence, the derived measurements of the turbulence are contaminated by the turbulence produced at the telescope dome (designed as dome seeing). The proper knowledge of the atmospheric turbulence (without any other turbulence contribution as dome seeing) is essential for the development of efficient adaptive optive systems and, in particular, to multi-conjugated adaptive optic systems for the forthcoming Extremely Large Telescopes (ELTs). We have developed a specific procedure to identify and remove the dome seeing from Generalized SCIDAR observations based on the evenness properties of the Fourier transforms (Fuensalida, García-Lorenzo & Hoegemann 2007). The procedure is fast and fully automated, being able to obtain the atmospheric turbulence profiles (without dome seeing) from G-SCIDAR measurement in near real time.

2. Implementation of the procedure

The algorithm to remove the dome seeing contribution starts with the slice y=0 of the autocorrelation function of the G-SCIDAR frames. Let f_i(x,y) be a specific frame. The autocorrelation due to atmospheric turbulence (outside the telescope dome) can be written as $[f_i * f_i]_L = [f_i * f_i] - [f_i * f_i]_d$, where the first term is the complete autocorrelation function of the frames provided by G-SCIDAR observations, and the second is the autocorrelation due to the dome seeing.

In spite of a small de-correlation of the dome seeing among successive frames, we treat this effect making use of cross-correlation series of five consecutive frames. Although the de-correlation of the dome seeing among successive frames is very small, we treat this effect using cross-correlation series of five consecutive frames. Let $[f_i * f_{i+j}]$ (being j=1,2,3,4,5) the series of five cross-correlations. The temporal interval between the two of function is jΔt. The interval should be sufficiently small to ensure that $f_{L,j\Delta} (x , y) = \Sigma f_l (x + jx_l , y + jy_l)$ for larger values of j. Furthermore, the dome seeing signature at cross-correlations (dome seeing triplet) could be partially overlapped by the signature (triplets) of certain layers in the cross-correlations for smaller values of j. We have define a function g(x,y) to take into account the shape of the scintillation speckles, g_l (x,y) and g_d (x,y) for the atmospheric layers and dome contribution, respectively. If Γ_l is the full width half maximum (FWHM) of g_l (x,y) and Γ_d is the same for g_d(x,y), and s_l is the separation of the lateral peaks of triplets respect the central one. Therefore, the velocity of the layer $v_l = (u_l,0)$, in order to avoid this effect should be $u_l \geq 2s_l + (\Gamma_l - \Gamma_d)/(2j \Delta t)$, but if $v_l = (0, v_l)$, the condition should be $u_l \geq \Gamma_l / j \Delta t$. In practice, we use the cross-correlation with j = 4 to get the shape of $[f_i * f_i]_d$, so we should avoid the occasional conditions when the lowest layers could dramatically affect the dome contribution. Consequently, we assume that $[f_i * f_i]_d = q [f_i * f_{i+4}]_d$, where q is obtained from a linear regression fit among the maxima M_j of the part of the dome seeing of the five cross-correlations $[f_i * f_{i+j}]_d$. Let **b** and **m** be the independent parameter and slope of the fitting, respectively (this is: $q = b/m_4$). In general, the m values are very small, which indicates a slight de-correlation of the dome seeing between succesive cross-correlations. We then obtain the net profile P_L(x) with the slices of the autocorrelation free of dome seeing $P_L (x) = [f_i * f_i]_L (x,0) - [f_i * f_i]_L (0,y)$ which is the input to the inversion algorithm for deriving the strength of the detected turbulence layers. The complete procedure is fast and it has been implemented to remove t

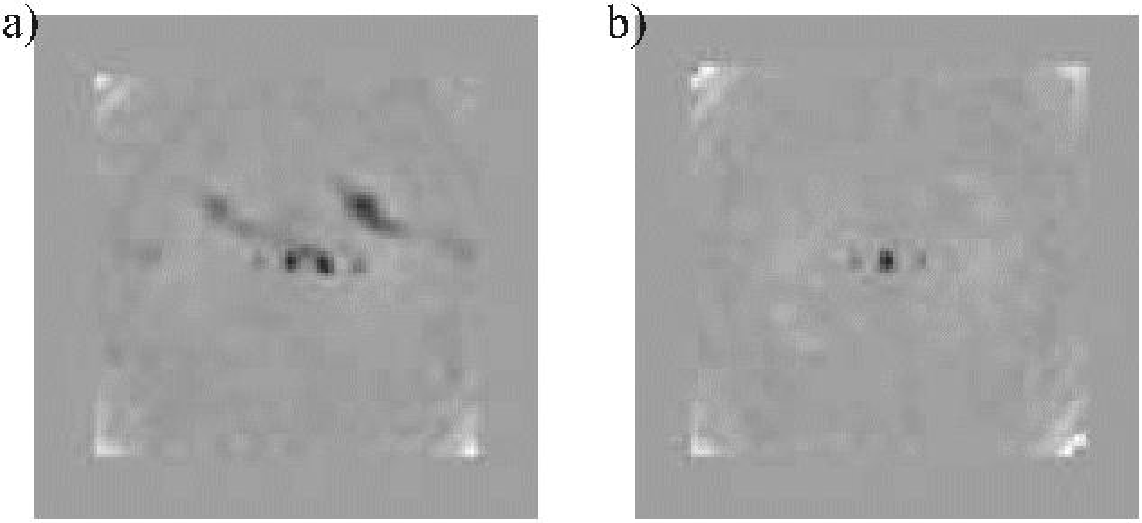

FIG. 1. Example of an experimental case in critical conditions to obtain the dome seeing contribution. (a) The first cross-correlation of a real G-SCIDAR data ([f_i * f_{i+1}]). A low altitude turbulent layer is moving in the direction of the alignment of the binary star and its triplet pattern overlaps the triplet corresponding to dome seeing. (b) The dome seeing contribution resulting from applying the procedure to the frame in (a).

the dome seeing in real time in the new G-SCIDAR instrument installed in Paranal (see Delgado et al. in this proceedings). Figure 1 shows the results obtained with observational data.

3. Validation of the procedure

In order to study the reliability of the developed procedure, we have compared (see Fig. 2) the seeing derived from G-SCIDAR profiles with data from ROBODIMM (ROBODIMM is an automatic seeing monitor operated by the Isaac Newton group of Telescopes and it is located at around 400 m from the Jacobous Kaptein Telescope, where G-SCIDAR data for this validation were obtained). The turbulence profiles have been integrated to derived seeig values before and after the dome seeing contribution was removed using the proposed algorithm. Data for validation are from the Roque de los Muchachos observatory (Spain).

4. Conclusions

We have developed a relatively simple procedure for correcting the G-SCIDAR measurements to obtain C_N^2(h) profiles from the dome seeing contribution. The procedure uses five consecutive cross-correlations and it is based on the shape recognition of the autocorrelation function of the turbulence produce inside the telescope dome. Results are in excellent agreement with DIMM measurements.

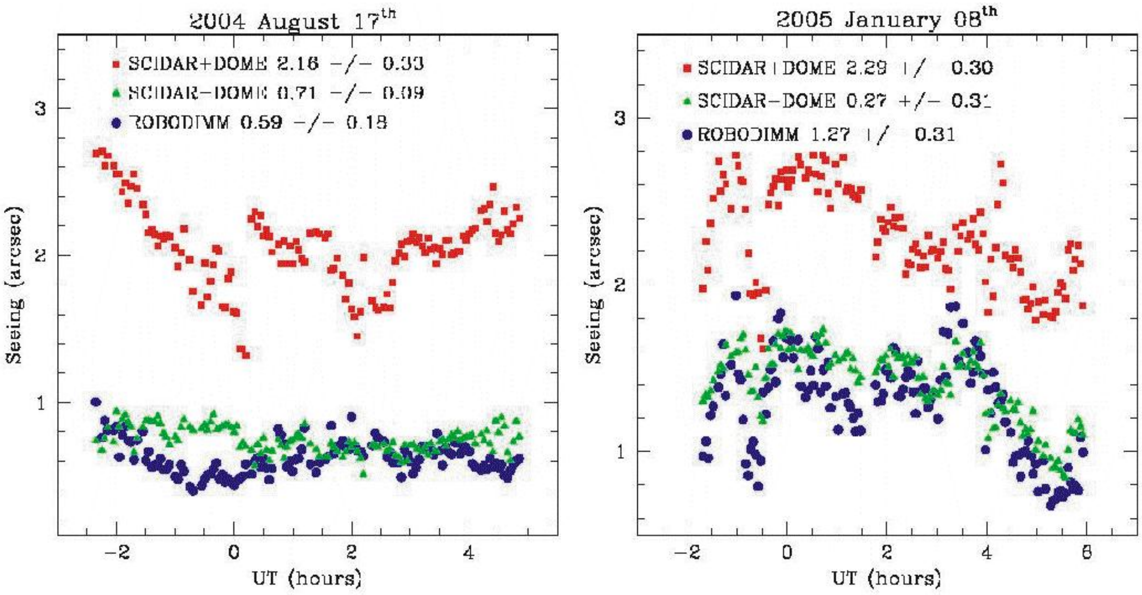

FIG. 2. Comparison between seeing size provided by ROBODIMM (blue filled circles) and those obtained from G-SCIDAR measurements for the nights (left-panel) 17/18 August 2004, and (right-panel) 08/09 January 2005. Red filled squares correspond to the seeing values derived from turbulence profiles including the dome seeing contribution. Green filled triangles are the seeing once the dome seeing contribution was removed using the proposed procedure. The mean and the standard deviation of measurements are indicated. The discrepancies are within the variations provided by the surface layer effect at the observatory

Acknowledgments.

The Jacobous Kapstein Telescope and the ROBODIMM are operated by the Isaac Newton Group at the Observatorio del Roque de los Muchachos (La Palma, Spain) of the Instituto de Astrofísica de Canarias. The authors thank all the staff at the observatory for their kind support. We also thank A. Eff-Darwich for help and useful discussions. This work was partially funded by the Instituto de Astrofísica de Canarias and by the Spanish Ministerio de Educación y Ciencia (AYA2006-13682).

References

Fuchs, A., Tallon, M., & Vernin, J. 1994, Proc.SPIE,2222,682

Fuensalida, J.J., García-Lorenzo, B., & Hoegemann 2007, to be sent to MNRAS

Johnston, R.A., Dainty, C., Wooder, N., & Lane, R. 2002, Appl.Opt., 41, 6768

Kluckers, V., Wooder, N., Adcock, M., & Dainty, C. 1998, A&ASuppl.Ser., 130, 141

Rocca, A., Roddier, F., & Vernin, J. 1974, J.Opt.Soc.Am., 64, 1000

Vernin, J. & Roddier, F. 1973, J.Opt.Soc.Am., 63, 270

Determination of the velocity vector of turbulence layers from G-SCIDAR observations using an algorithm based on wavelet transforms

Begoña García-Lorenzo* and Jesús J. Fuensalida
Instituto de Astrofísica de Canarias, Tenerife, Spain

ABSTRACT

The G-SCIDAR data processing for the determination of the magnitude and direction of the wind requires an efficient and contrasted code. We have developed a fully automated algorithm based on wavelet transforms to derive the wind velocity of atmospheric turbulent layers from Generalized SCIDAR measurements. The algorithm makes use of five cross-correlations of a series of scintillation patterns separated by lapses of Δt, 2Δt, 3Δt, 4Δt and 5Δt. The analysis is performed using wavelet and provides the position, direction and altitude of the different turbulent layers detected in each of the five cross-correlations. The comparison and consistency of results in consecutive cross-correlations allows the determination of the velocity of turbulence layers and avoids misidentifications associated with noise and/or overlapping layers. The software takes into account the projection effects on the observing direction of the actual velocity vector of turbulence layers. We have applied the algorithm to simulated data with excellent results. Velocities derived from actual G-SCIDAR observations are compared to the velocities provided by balloon measurements. Our software has been designed to analyze huge amounts of G-SCIDAR measurements.

Corresponding author address: Begoña García-Lorenzo Instituto de Astrofísica de Canarias, C/ Via Lactea S/N, 38200-La Laguna, Tenerife, Spain.
E-mail: bgarcia@iac.es

1. Brief introduction to wavelets

Wavelet analysis is based on the decomposition of data into different components, through mathematical functions called wavelets, allowing the study of each component separately. The wavelet-based analysis transforms a one-dimensional function into a 2-D parameter space. In this sense, the wavelet transform translates and dilates a function (mother wavelet), convolves it with the signal to be analyzed and studies the coefficients in the translation and dilation space (wavelet space). The cross-correlation images (CC(Z,Y) hereafter) of G-SCIDAR data provide the information to determine the velocity of the turbulent layers (see Fig. 1). In order to apply the wavelet-based analysis, the CC(Z,Y) should be transformed into 1-D functions sitting the different lines of the CC(Z,Y) images consecutively. In this way, we transform the YxZ cross-correlation image (CC(Y,Z)) into a 1-D function, F(X), of YxZ elements (García-Lorenzo & Fuensalida 2006a). When the wavelet transform is applied, using a Morlet function as the mother wavelet, we obtain a 2D function, W(t,d), in the wavelet space. The brightest peaks in W(t,d) are related to the triplets in CC(X,Y), and hence give information about turbulence layers. The translation parameter (t) is related to the position X in the F(X) function and, therefore, with the coordinates (Y,Z) in CC(Y,Z), giving the velocity and direction of turbulence layers. The dilation parameter (d) is related to the separation of lateral peaks relative to the central peak of the triplets in CC(Y,Z), and hence, to the altitude of the turbulence layers. The wavelet power spectrum can also present several secondary peaks that are not associated to turbulent layers, since they correspond to harmonic frequencies of the brightest peaks. The comparison with triplets in Fig. 1(a) reveals that these harmonic frequencies do not correspond to a real triplet (turbulent layers).

2. Deriving turbulence layer velocities using wavelets

G-SCIDAR observations can provide CC(Y,Z) images at different lapses of time. If these lapses are short enough, different triplets in CC(Y,Z) could be overlapped, whereas for large enough lapses, triplets associated to relatively high velocity turbulent layers could disappear in CC(Y,Z) (see Fig. 1). The procedure that we propose in this work consists of extracting the velocity and altitude of turbulent layers by the consistence of its displacements in consecutive cross-correlation images taken at five lapses of time (1Δt, 2Δt, 3Δt, 4Δt, 5Δt). The program starts analyzing the CC(Y,Z) at 5Δt (CC5, hereafter) using the wavelet-based algorithm. The translation and dilation parameters indicating peaks in the wavelet power spectrum associated to CC5 are compared to triplets in CC5 in order to discard any peak associated to harmonic frequencies and/or noise. We applied the same procedure to CC(Y,Z) at 4Δt (CC4 hereafter) and 3Δt (CC3 hereafter). At this step, we move the coordinates of the different peaks obtained from the analysis of the wavelet power spectrum associated to CC5, CC4, and CC3 to 3Δt using the relationship: Velocity=Space/Time. Comparing the three set of parameters, we determine the coordinates associated to common triplets in CC5, CC4 and CC3 (true triplets). Following the same procedure, the algorithm compares the parameters in the wavelet space obtained for CC4, CC3, and CC2, and then CC3, CC2, and CC1 moving these parameters to 3Δt. Finally, we compared the triplets identified in CC2 and CC1, recalling that in real G-SCIDAR observations there may be peak blending in CC1 and CC2. At the end, we have a set of parameters associated to turbulent layers, being their velocities, directions and altitudes consistent with the five cross-correlation images.

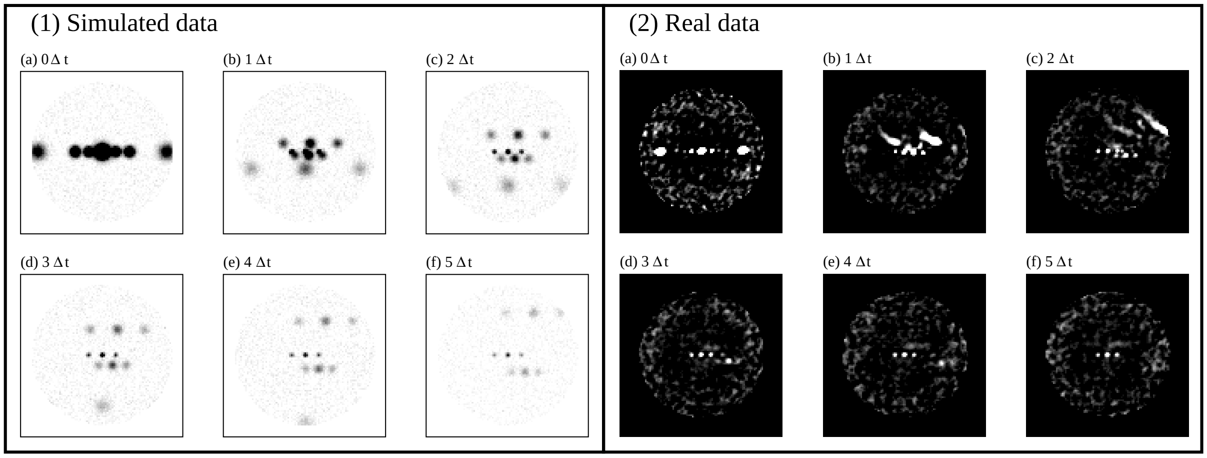

FIG. 1. **(1) Simulated data:** Simulation of the cross-correlation images of scintillation patterns produced by four turbulent layers on the light coming from a binary star at the telescope pupil, separated by the lapses of time indicated in each plot. When lapse is 0Δt, (1a), the average normalized autocorrelation is obtained. For lapses 1Δt, (1b), and 2Δt, (1c), triplets associated to different turbulent layers are overlapped. When lapses are larger than 3Δt, (1d),(1e), and (1f) triplets are well separated. **(2) Real data:** (2a) The average normalized autocorrelation of 1000 scintillation patterns observed at the 1m Carlos Sánchez Telescope pupil (Teide Observatory, Spain) produced by turbulent layers on the light coming from the binary star BS7948 on the night of 2003/08/31 at $\sim$23 UT; Cross-correlation of the same series of scintillation images as (2a) but separated by a lapse of (2b) Δt=26 ms; (2c) 2Δt=52 ms; (2d) 3Δt=78 ms; (2e) 4Δt=104 ms; (2f) 5Δt=130 ms. Each triplet in these images gives information about the intensity, altitude and velocity of each turbulent layer. The triplet at the center of each plot corresponds to the turbulence produced at the dome (V=0).

3. Application of the algorithm to simulated and real G-SCIDAR data

In order to verify the wavelet-based procedure, we have applied the software to the simulated and real data in Fig. 1(a) and 1(b) (see García-Lorenzo & Fuensalida2006a,b). Fig. 2 shows the C_N^2 profile obtained from simulated data assuming the observation conditions of the SCIDAR instrument (called *Cute*-SCIDAR) installed at the Roque de los Muchachos Observatory on the island of La Palma (Spain). Fig. 3 shows the the results derived from G-SCIDAR data obtained at the Carlos Sánchez Telescope installed at the Teide Observatory on the island of Tenerife (Spain) during the night 2003 August 31.

Acknowledgments.

The authors thank A. Eff-Darwich for useful discussions. Wavelet software was provided by C. Torrence and G. Compo (http://paos.colorado.edu/research/wavelets/). The Carlos Sánchez Telescope is operated by the Instituto de Astrofísica de Canarias at the Teide Observatory (Tenerfie, Spain). The authors thank all the staff at the observatory for their kind support. This work was partially funded by the Instituto de Astrofísica de Canarias and by the Spanish Ministerio de Educación y Ciencia (AYA2006-13682).

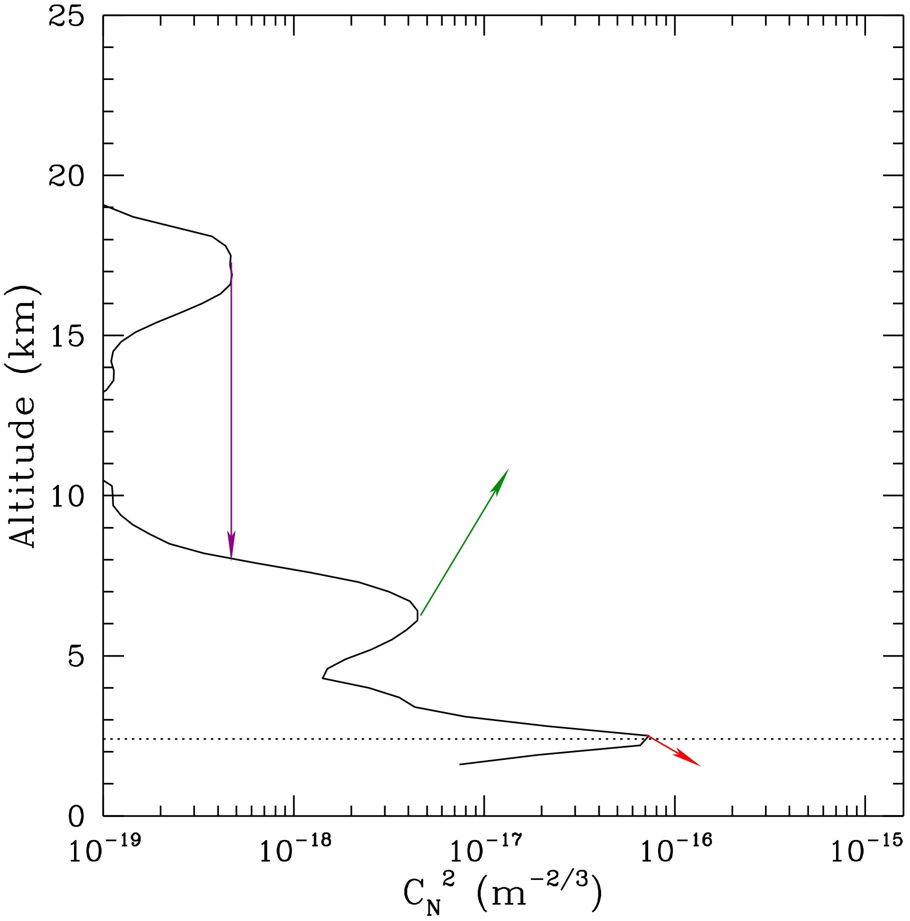

FIG. 2. C_N^2 profile obtained from the simulated data. We have assumed a G-SCIDAR set-up similar to the Cute-SCIDAR installed at the Observatorio del Roque de los Muchachos. The dome seeing contribution has not been removed from the profile. The size of the arrows indicates the velocity module associated to each turbulent layer in the simulation. Arrows indicate the wind direction in Cartesian coordinates. The velocity of the turbulent layer associated to the dome is zero and it has not been drawn in this plot. The total seeing from the turbulence profile is 1.64 arcsec (including dome contribution) and the isoplanatic angle obtained from this profile is 1.94 arcsec. (see García-Lorenzo & Fuensalida 2006b for more details).

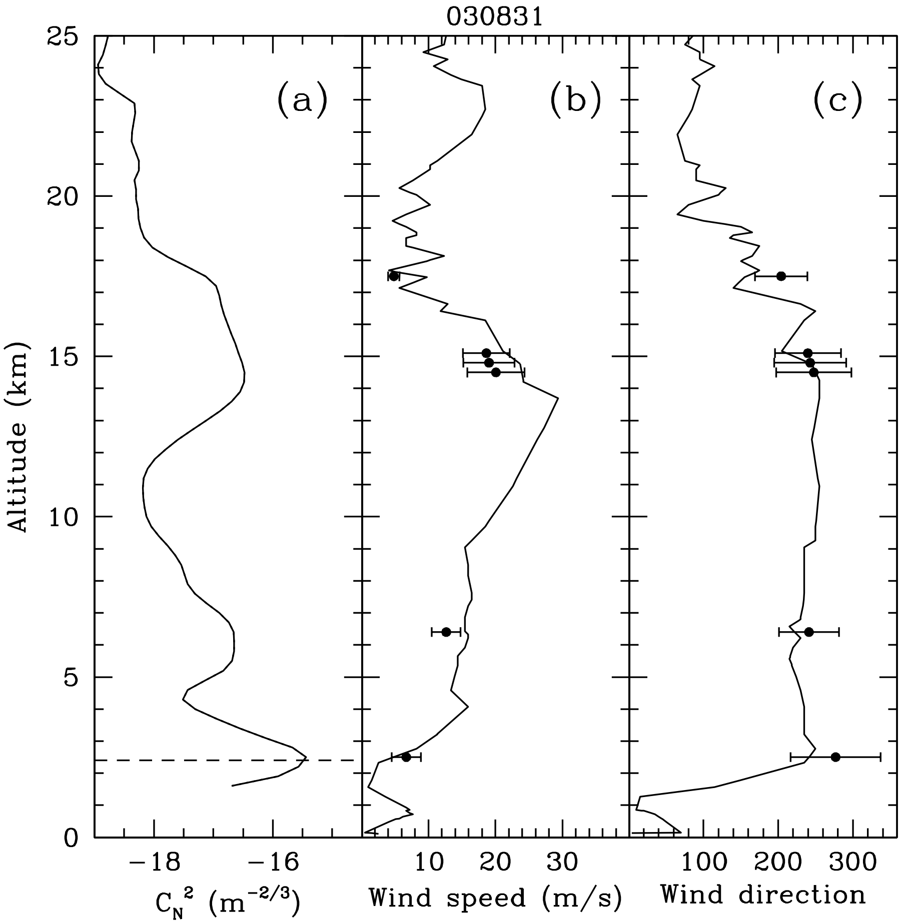

FIG. 3. Results derived from real G-SCIDAR data in FIG.1 using the wavelet-based algorithm. (a) The average of the C_N^2 measurements (130 individual profiles) derived from G-SCIDAR data during the corresponding balloon ascent. The horizontal dashed line indicates the observatory altitude (2400 m). Dome seeing has been removed from the profiles using a procedure based on the properties of the parity of functions. (b)Wind vertical profile. The solid line corresponds to wind speed measurements with radiosondes launched 13 km away from the observatory. Filled circles are the derived velocities for turbulent layers from G-SCIDAR data. Error bars indicate the standard deviation of the G-SCIDAR measurements during the corresponding balloon ascent. (c) The same as (b) but for the wind direction. (see García-Lorenzo & Fuensalida 2006a for more details).

References

García-Lorenzo, B., & Fuensalida, J.J. 2006, MNRAS, 372, 1483-1495

García-Lorenzo, B., & Fuensalida, J.J. 2006, SPIE, 6267, 61

Evaluation of projection effects in the determination of the velocity vector of turbulent layers from G-SCIDAR observations

Begoña García-Lorenzo* and Jesús J. Fuensalida
Instituto de Astrofísica de Canarias, Tenerife, Spain

ABSTRACT

G-SCIDAR observations provide the atmospheric turbulence profile (C_N^2(h)) and the velocity vector associated to each detected turbulent layer. The velocity derived from G-SCIDAR is in fact the projection of the real layer velocity vector on the plane perpendicular to the observing direction. The effects of such projection on the determination of velocity vectors have been assumed to be relatively small as the G-SCIDAR data are normally obtained at zenith angles smaller than 30 degrees. We have calculated the mathematical expression for the error in the determination of the wind direction and modulus from G-SCIDAR data due to such projection and assuming a turbulent layer moving horizontally. We also give results about the effects for some observational cases.

---

* *Corresponding author address:* Begoña García-Lorenzo, Instituto de Astrofísica de Canarias, C/ Via Lactea S/N, 38200-La Laguna, Tenerife, Spain.
E-mail: bgarcia@iac.es

1. Introduction

G-SCIDAR (Generalized SCIntillation Detection And Ranging) is a remote-sensing technique to measure the strength and velocity of the atmospheric turbulence layers. The method is based on the analysis of the scintillation patterns produced at the telescope pupil by the light coming from the stars in a binary system (for a detail description of the technique see e.g. Kluckers et al 1998 and references therein). The velocity derived from G-SCIDAR observations corresponds to the projection of the turbulence layer velocity vector on a plane perpendicular to the observing direction defined by the telescope zenithal distance . Here, we calculate the mathematical expression for the error in the determination of the velocity vector (direction and modulus) from G-SCIDAR due to such projection and assuming a turbulent layer moving horizontally.

2. Formulation

Let XYZ be a tree-dimensional coordinate system. The axes are selected in a world-coordinates orientation with the Z-axis pointing up, representing the zenith direction for an astronomical observatory. If we are observing with a G-SCIDAR instrument a particular source at a Zenithal distance Θ, we can define a second 3D coordinate system, X'Y'Z'. Such a coordinate system can be selected as a coordinate system rotated about the X-axis, and then, X'Y'Z'$\equiv$ XY'Z'. In this way, the Z'-axis represents the observing direction and Z'-axis forms an angle Θ with the Z-axis, while the Y'-axis corresponds to the azimuth direction of the observation. Figure 1 shows an squeme of the XYZ and XY'Z' coordinate systems.

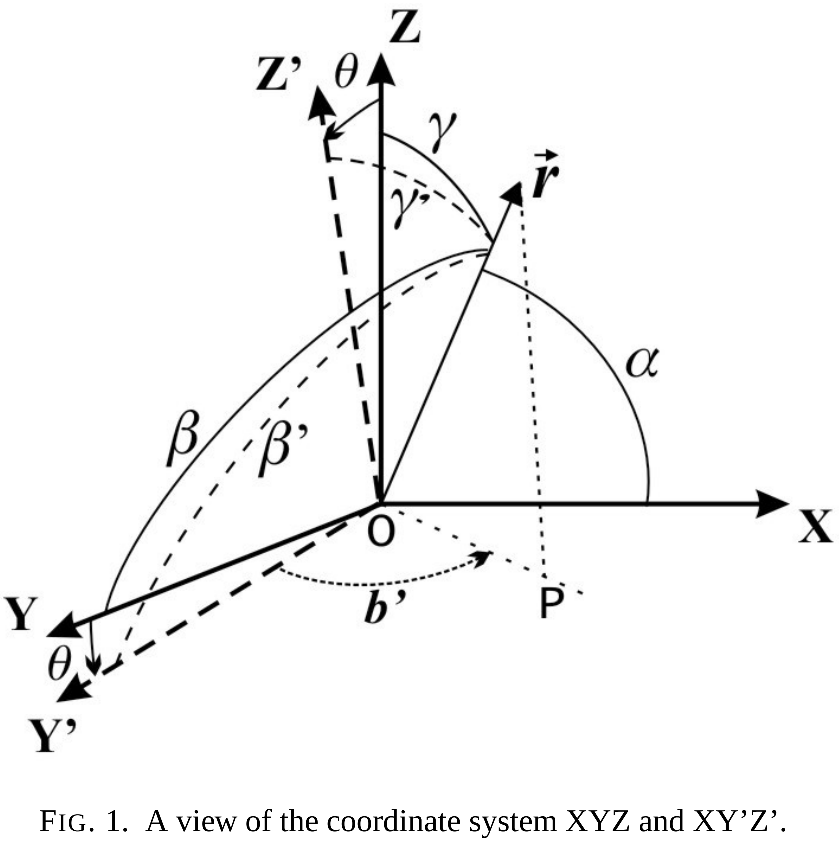

FIG. 1. A view of the coordinate system XYZ and XY'Z'.

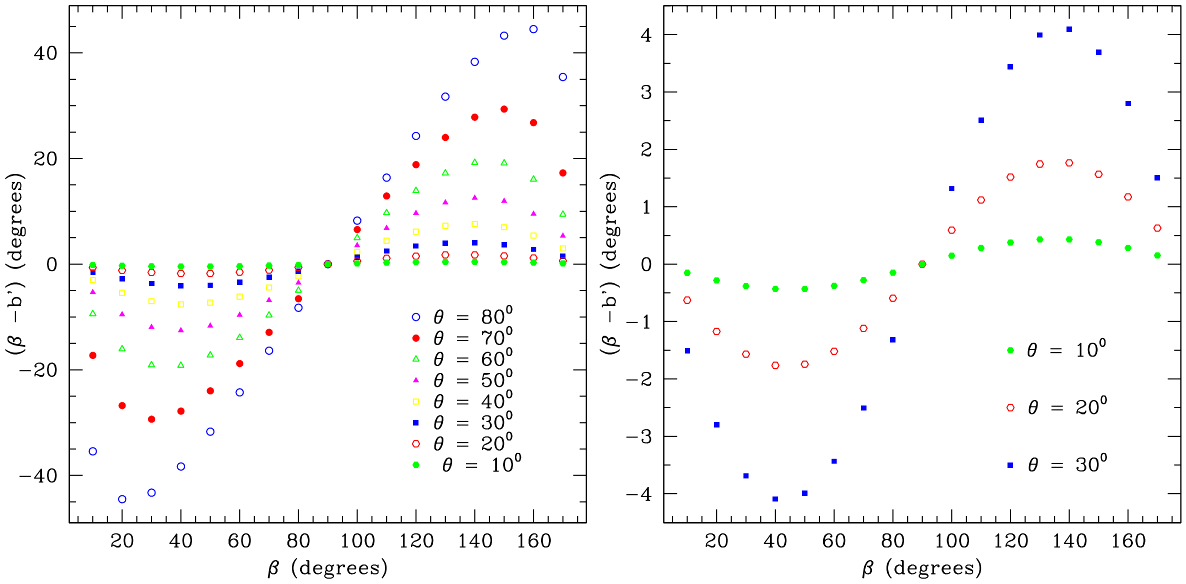

FIG. 2. (left-panel) Error in the determination of wind direction from G-SCIDAR measurements as a function of the actual direction of the velocity vector of a particular turbulent layer. Different symbols correspond to different zenith angles (different observing directions). (right-panel) The same as (left-panel) but for zenith angles smaller than 30deg, which is the usual situation in G-SCIDAR observations.

Let (l_y, m_y, n_y) and (l_z, m_z, n_z) be the direction cosines of the Y' and Z' axis, respectively, in the XY'Z' system expressed in function of X, Y, and Z in the XYZ-system. Then,

$$y' = l_y x + m_y y + n_y z \Longrightarrow y' = cos\Theta y - sin\Theta z \tag{1}$$

$$z' = l_y x + m_y y + n_y z \Longrightarrow y' = cos\Theta y - sin\Theta z \tag{2}$$

The direction of any vector **r** is determined by its direction cosines, given by (cos α, cos β, cos γ) in the XYZ-system, and (cos α, cos β', cos γ') in the XY'Z'-system (see Fig. 1):

$$x_r = |\mathbf{r}|cos\alpha, \qquad y_r = |\mathbf{r}|cos\beta, \qquad z_r = |\mathbf{r}|cos\gamma \tag{3}$$

$$x'_r = |\mathbf{r}|cos\alpha', \qquad y'_r = |\mathbf{r}|cos\beta', \qquad z'_r = |\mathbf{r}|cos\gamma' \tag{4}$$

From equations 1-4, we obtain:

$$cos\beta' = cos\Theta cos\beta - sin\Theta cos\gamma \tag{5}$$

$$cos\gamma' = sin\Theta cos\beta + cos\Theta cos\gamma \tag{6}$$

Applying the law of cosines to the spherical triangle forms by the projection of the vector **r** on the XY'-plane (OP segment in Fig. 1), the vector **r** itself and the Y'-axis (see Fig. 1), we can write:

$$cos\beta' = cosb' sin\gamma' \tag{7}$$

From equations (5) and (7), we obtain:

$$cosb' = \frac{cos\beta cos\Theta - cos\gamma sin\Theta}{\sqrt{1-(cos\beta sin\Theta + cos\gamma cos\Theta)^2}} \tag{8}$$

For a plane-parallel atmosphere, any turbulent layer will be in the XY plane, and therefore, $\gamma = 90^o$. In this case, equation (8) can be written as:

$$cosb' = \frac{cos\beta cos\Theta}{\sqrt{1-cos^2\beta sin^2\Theta}} \tag{9}$$

where β corresponds to the direction of the turbulent layer motion referred to the azimuth direction.

3. Observational cases

a. Effects on the direction

If a binary star is observed in the direction Z' using the G-SCIDAR technique, the detected direction is the projection in the XY' plane fixed by the b' angle. Therefore, the error is the difference between β and b' and it is given by:

$$(\beta - b')_{rad} = \beta - arccos(\frac{cos\beta cos\Theta}{\sqrt{1-cos^2\beta sin^2\Theta}} \tag{10}$$

Figure 2 shows the differences between a turbulent layer velocity direction and the wind direction determined from G-SCIDAR observations for different zenithal distances (Θ). For zenith angles smaller than 30^o, such differences are always smaller than 4^o. In general, G-SCIDAR observations are carried out at zenith angles smaller than 30^o (this is always the case for G-SCIDAR instruments installed at the Canary Islands observatories) and, therefore, uncertanties due to projection effects are almost negligible.

b. Effects on the modulus

The projection of the velocity vector on the plane perpendicular to the observing direction also affects to the determination of the velocity module. The projection of | r | $\equiv$ r on the XY'-plane is the segment OP $\equiv$ **r**' (see Fig. 1), then:

$$r' = rsin\gamma' \tag{11}$$

Using equations (5), (7), and (9), and taking into account the assumption $\gamma = 90\deg$ for G-SCIDAR measurements, we derive:

$$\frac{r'}{r} = \sqrt{1-cos^2\beta sin^2\Theta} \tag{12}$$

Figure 3 shows the percentage errors when determining the wind moduli from G-SCIDAR measurements for different zenith angles. The maximum error is reached when the velocity vector is along the azimuth direction, $\beta = 0\deg$ or $\beta = 180\deg$. Percent errors smaller than 14% (see Fig. 3) are archived when observing with zenith angles smaller than $30\deg$, which is the typical situation in G-SCIDAR observations. Therefore, the projection effects could be an important source of uncertanties when determining the velocity modulus.

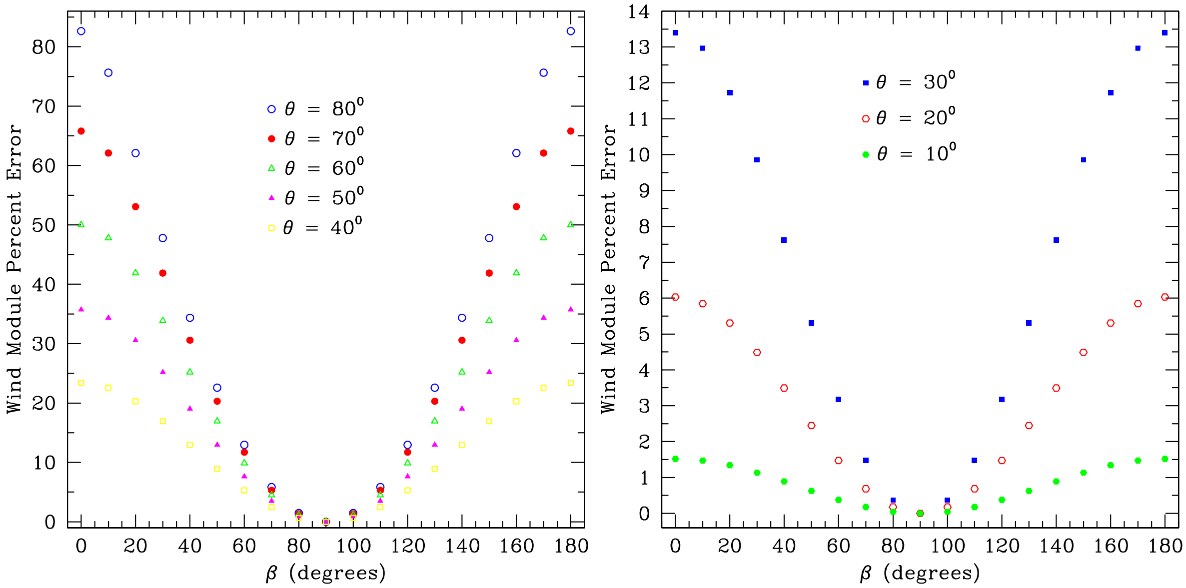

FIG. 3. (left-panel) Percentage error in the determination of wind modulus from G-SCIDAR data as a function of the actual direction of the velocity vector of a particular turbulent layer. Different symbols correspond to different observing directions (zenith angles). (right-panel) The same as (left-panel) but for zenith angles smaller than 30deg, which is the usual situation in G-SCIDAR observations.

Acknowledgments.

The authors thank A. Eff-Darwich for useful discussions. This work was partially funded by the Instituto de Astrofísica de Canarias and by the Spanish Ministerio de Educación y Ciencia (AYA2006-13682).

References

García-Lorenzo, B., & Fuensalida, J.J. 2006, MNRAS, 372, 1483-1495

DIMMA: a completely unmanned Differential Image Motion Monitor

Antonia M. Varela*, Luis Fernando Rodríguez, Casiana Muñoz-Tuñón
Instituto de Astrofísica de Canarias, Tenerife, Spain

and

Miguel Sosa
INERZA, S.A.., Gran Canaria. Canary Islands. Spain

ABSTRACT

Both astronomical site selection and design for the next future large telescopes, plus the need to define flexible schedule programs as operational schemes for the telescopes at the observatory require systematic measurements of the night-seeing and meteorology. The first completely unmanned Differential Image Motion Monitor Automático (DIMMA) has been developed by the Sky Quality Group of the IAC and installed at the Roque de los Muchachos Observatory (La Palma, Spain) in summer 2006. DIMMA operation does not require man power for operation, it is powered by solar panels and linked via internet to the rest of the world, allowing to obtain and to supervise meteorological and seeing data from remote sites.

---

*Corresponding author address: Antonia M. Varela, Instituto de Astrofísica de Canarias, C./Via Láctea, S/N, 38200-La Laguna, Tenerife, Canary Islands, Spain
E-mail: avp@iac.es

1. Introduction

The DIMMA system (Differential Image Motion Monitor Automático) is the natural step forward in the telescope-based equipments used for site evaluation in astrophysics. Using the experience and know-how of the DIMM systems (Vernin & Muñoz-Tuñón, 1992) regularly operated since 1995 at IAC by the Sky Quality Group, the DIMMA provides a comprehensive set of data without the need of any manned operation, in close linkage with the rest of the world using internet.

The scientific base of DIMM is to separate two light beams coming from the same star but received in two separate zones of the primary mirror (telescope aperture). This task is accomplished covering completely the telescope aperture except for two small apertures. The light going through one of the apertures will be slightly deviated by a prism, thus obtaining two images of the same star in the focal plane. Seeing data can be computed from the variance of the distance between the two images, in both the horizontal and vertical axis, Sarazin and Roddier (1990); Vernin and Muñoz-Tuñón (1995).

A number of system based on this scheme are presently installed in most astrophysical observatories, and are being routinely used for site surveys. The DIMMA system is inspired in the following features:

- Completely automatic. No operator needed.
- Using ideas and previous developments of earlier DIMMs.
- Completely outsourced, if possible.
- Use as many commercial off the shelf products as possible
- To be place in remote sites, with no infrastructure at all.
- Powered using only photovoltaic solar energy
- Designed to be copied about a dozen times
- Capable of storing all relevant data, including housekeeping, seeing and weather
- Featuring a built in software data quality checking module.
- Use a number of already available subsystems.

2. Status of the DIMMA

DIMMA was developed by the firm INERZA, S.A. (Las Palmas de Gran Canaria, Spain) under contract by IAC. In June 2006 has started the DIMMA installation at the ORM at Las Lajitas (see Figure 1). The DIMMA has been mounted on a 5m tower avoiding the surface layer effect on the seeing measurements. Next to the tower we have installed an Automatic Weather Station consisting on a Data Acquisition Unit (DAU) and a lattice tower equipped by standard meteorological sensors. The weather parameters will be stored to be use for climatic analysis and will be also provided on-line for telescope operation control. Interface is shown is Figure 2. The DIMMA area has been fenced in order to guarantee the security of the station.

Fig. 1 DIMMA station at the ORM. The DIMMA is now under calibration and validation process and will be fully operative in spring 2007.

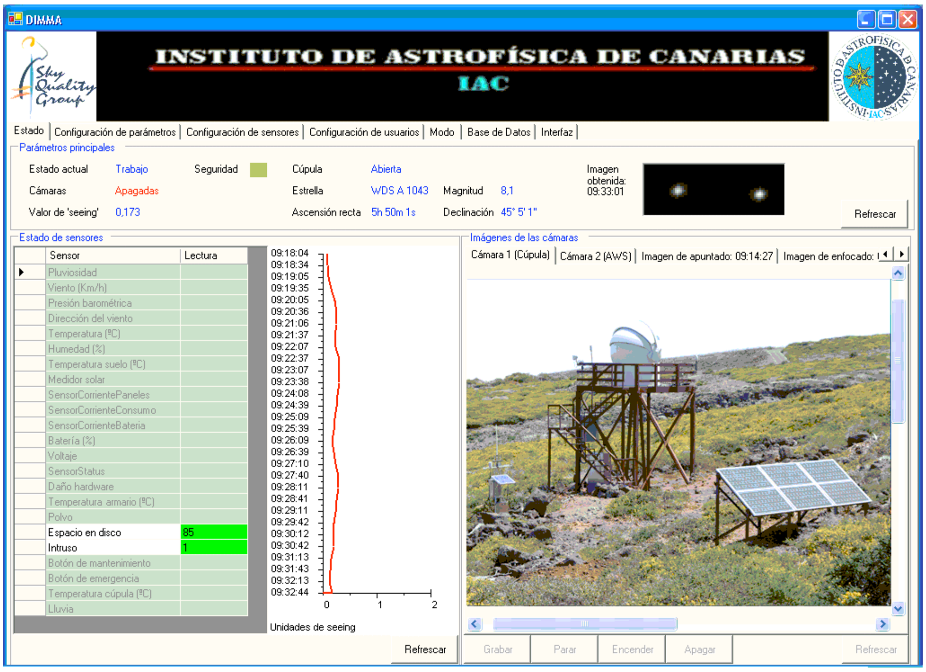

Estado actual Trabajo
Seguridad 🟩
Cúpula Abierta
Cámaras Apagadas
Estrella WDS A 1043
Magnitud 8,1
Valor de 'seeing' 0,173
Ascensión recta 5h 50m 1s
Declinación 45° 5' 1"
Imagen obtenida: 09:33:01

Sensor	Lectura
Pluviosidad	
Viento (Km/h)	
Presión barométrica	
Dirección del viento	
Temperatura (ºC)	
Humedad (%)	
Temperatura suelo (ºC)	
Medidor solar	
SensorCorrientePaneles	
SensorCorrienteConsumo	
SensorCorrienteBateria	
Batería (%)	
Voltaje	
SensorStatus	
Daño hardware	
Temperatura armario (ºC)	
Polvo	
Espacio en disco	85
Intruso	1
Botón de mantenimiento	
Botón de emergencia	
Temperatura cúpula (ºC)	
Lluvia	

Figure 2. DIMMA interface. There are two web cameras installed at the meteorological mast (see right image) and the other one inside the dome. The center window shows the seeing profiles along the night. Sensor and operation status information, observed stars, statistical seeing values, etc. are also included.

3. Main Characteristics

These are the main characteristics of the DIMMA:

- Separate supported personnel tower.
- Automatic point with less than 1 arc minute accuracy.
- Automatic focusing with two independent systems.
- Automatic dome opening and closing.
- Automatic weather station integrated within the control system.
- Web cameras for remote monitoring
- Multi-sensor integration for robotic control
- Database storage of both scientific and housekeeping data
- Wireless linked to the Ethernet
- Powered by solar panels (7.7m^2) plus batteries (2x450 Ah).

4. Block Diagram

In Figure 3 we represent the structure of the DIMMA system (instruments and communications, surveillance, control system and automatic weather station).

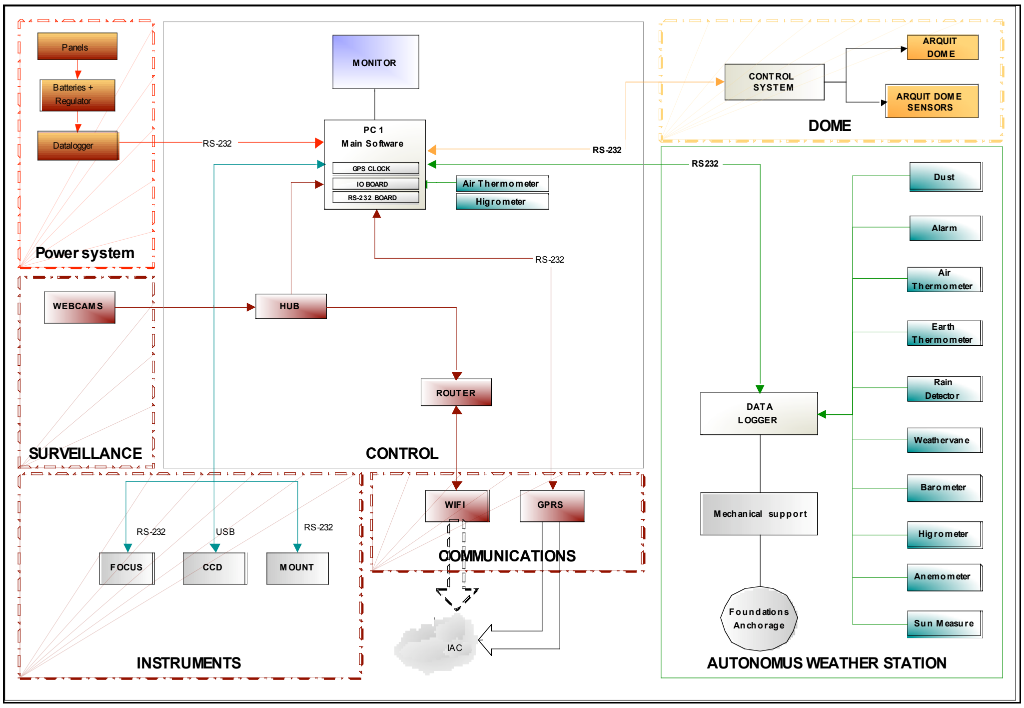

Fig. 3 Block Diagram showing all subsystems and their logical interconnections.

Acknowledgments.
This work has been carried out under the framework and funds of the European Project OPTICON as part of its specific objectives.

References

Muñoz-Tuñón, C., A.M. Varela and L.F. Rodríguez, 2004: Monitor de Seeing Automático (DIMMA). I Reunión Nacional de Astronomía Robótica. Huelva, Spain
Sarazin, M. and F. Roddier, 1990: A&A, 227,294
Vernin, J. and C. Muñoz-Tuñón, 1992: A&A, 257, 811
Vernin, J. and C. Muñoz-Tuñón, 1995: PASP, 107, 265

http://www.iac.es/project/sitesting/site.html
http://www.inerza.com/
http://www.otri.iac.es/na2/Annex7_NA2/WP21_M1.pdf

MASS-DIMM Setup at Palomar

Michael Thomsen*
Dept. Measurement & Instrumentation, Technical University of Denmark,

Matthew Britton and Andrew Pickles
Caltech Optical Observatories, Pasadena, California

ABSTRACT

We describe the implementation at Palomar Observatory of an automatic, robotic atmospheric turbulence monitoring system. The system is based on a 12 inch Meade RCX-400 telescope, coupled with a combined MASS-DIMM unit built at Tololo. The system operates every clear night and stores measurements of the vertical turbulence profile, along with derived turbulence parameters such as seeing, in a database. These values are available in real time to observers. The MASS information has been tested to accurately predict the field dependent point spread function from the Palomar Adaptive Optics System. These predictions have enabled enhanced photometry and astrometry with imaging detectors on the Hale 200-inch telescope. The information has also been used by observers to optimize observing strategies in response to seeing conditions, particularly during Adaptive Optics (AO) and Laser Guide Star (LGS-AO) observing runs.

**Corresponding author address:* Michael Thomsen, Technical University of Denmark, M&I, Building 327, 2800 Kgs. Lyngby, Denmark
E-mail: mt@oersted.dtu.dk

1. Introduction

Palomar Observatory currently hosts two robotic MASS-DIMM systems. The first is a version of the TMT site-testing equipment (T5) which has been operating on the roof of the power-house building at Palomar since May 2005. L. Wang, et al (2006), W. Skidmore et. al (2004). Although T5 is destined to go to another site, this system has demonstrated the utility of having access to detailed turbulence profiles, especially for comparison with our Adaptive Optics measurements and development of our Laser Guide Star Adaptive Optics program at http://www.astro.caltech.edu/oir/lgs/.

The new P18 system described here was installed in an existing (18-inch) dome in mid-2006. It is based on a combined MASS-DIMM unit (MD-18) built at Tololo and fed by a 12 inch Meade RCX-400 telescope. This system monitors Polaris and delivers real-time data every clear night at http://odata1.palomar.caltech.edu/massdimm/.

2. Sensors and Other Hardware

The MASS-DIMM instrument is a combination of a DIMM and a MASS sensor. MASS (MultiAperture Scintillation Sensor) measures four scintillation indices in a small central, circular aperture and 3 concentric annular apertures. From these are derived 6 differential scintillation indices for all possible pairs. Using these values it is possible to calculate some integral characteristics of the atmospheric turbulence and restore a low-resolution vertical turbulence profile with 5 to 6 layers. Note that the MASS does not sense turbulence in the boundary layer (lower 500 m above ground). A. Tokovinin (2006).

DIMM (Differential Image Motion Monitor) measures fluctuations of the angular distance between two images produced by two circular apertures about 10 cm in diameter separated by about 20 cm. The DIMM measures both low and high altitude turbulence along the complete line-of-sight, and therefore supplements the MASS unit well.

The DIMM system uses a SBIG ST5 camera with software running on Windows, while the MASS system uses custom electronics and software running on Linux. We therefore use two Little-PCs to control the system. Finally a remote computer grabs the seeing data and serves the data for the user community on a website. A block diagram of the hardware can be seen in the figure below.

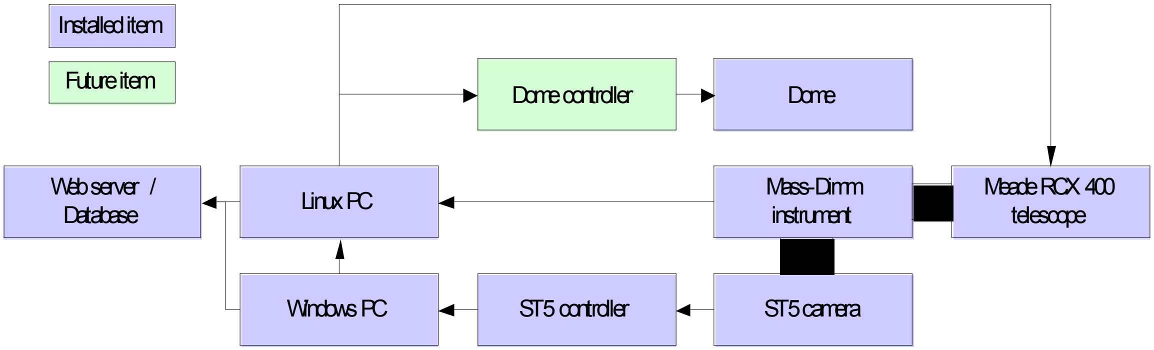

Fig. 1 Hardware block diagram

Installation Considerations

The RCX-400 telescope comes with a built-in GPS receiver. This is normally used to determine the geographic position for automatic aligning of the telescope and to provide accurate time for pointing; we use it for the latter function. Mounted on the telescope in the dome the GPS receiver often could not lock onto enough satellites. The GPS receiver is of the typical integrated type with patch antenna and all processing ICs mounted in a small package. The only connections required are power and serial I/O (9600 baud NMEA). It was therefore a simple task to extend the wires about 4 m and mount the GPS receiver in the top of the dome, just below the dome shutters, with a clear view of the sky when the dome is open. This proved to be an excellent solution giving fast lock on the GPS signals.

The 18-inch dome is being upgraded for automatic, remote open/close functionality. It closes automatically in the event of a bad weather signal from one of the other telescope weather systems, and resets itself to be capable of opening when the weather clears. The local supervisor computer checks and reopens the dome when it can. The dome rotation function is unreliable for this older dome, and an early decision was made to restrict observations to a single target: Polaris.

Prior to observations, the telescope coordinates need to be calibrated. Once done, this calibration will work for weeks or months unless power is lost to the telescope. We normally leave the telescope tracking on Polaris at all time, but perform a slew and re-acquisition search at the start of observing each night. To calibrate the coordinates, we perform the standard Meade 2-star alignment on stars relatively near our target of Polaris. The Meade position readout in RA/Dec is based on an expansion of the Alt/AZ coordinates actually used for tracking. This has the unfortunate consequence that RA/Dec coordinates near the pole are NOT constant, but increment gradually and then cycle back, while the telescope tracks quite well in Alt/Az. After the standard Meade alignment, we therefore slew to Polaris, center on the DIMM image, note the average coordinates, and update our target coordinates slightly to those closest to the current alignment.

Telescope slews are unfortunately not accurate enough to consistently recover Polaris within the DIMM/ST5 field (about 2-arcmin). After opening each clear night at 10-degree twilight, the automatic system slews the telescope to Polaris, performs a spiral search pattern until the star shows up and is recognized by the software in the DIMM field. It then offsets for MASS background measurement, then re-acquires Polaris to start observations. Re-acquisition is again necessary if the dome closes and re-opens because of weather, but is normally achieved within 10-15 minutes.

3. Software

The software consists of the following programs, also shown in a block diagram in figure 2:

- RoboDIMMnet (Windows) - measures the DIMM seeing using the ST5 camera
- Turbina (Linux) - controls the MASS instrument and computes the seeing profile
- OBJM (Linux) - selects the optimal star to monitor from a small database (currently only Polaris is in the P18-MD OBJM database)
- TLSP (Linux) - telescope control software
- Supervisor (Linux) - starts and stops observations, and controls the measurement cycle

The Windows computer runs a modified version of RoboDIMMnet v1.5.2 used to control the DIMM instrument. The modification consists of outputting a daily ASCII data file with date, time and seeing data. The distance between the center of the two images of the star and the center of the DIMM CCD is transferred to the Supervisor, which then moves the telescope so the star becomes centered on the CCD. If the star is not in the field of view after slewing to the star, the Supervisor will perform a spiral search to find it. If the star is lost another spiral search is executed.

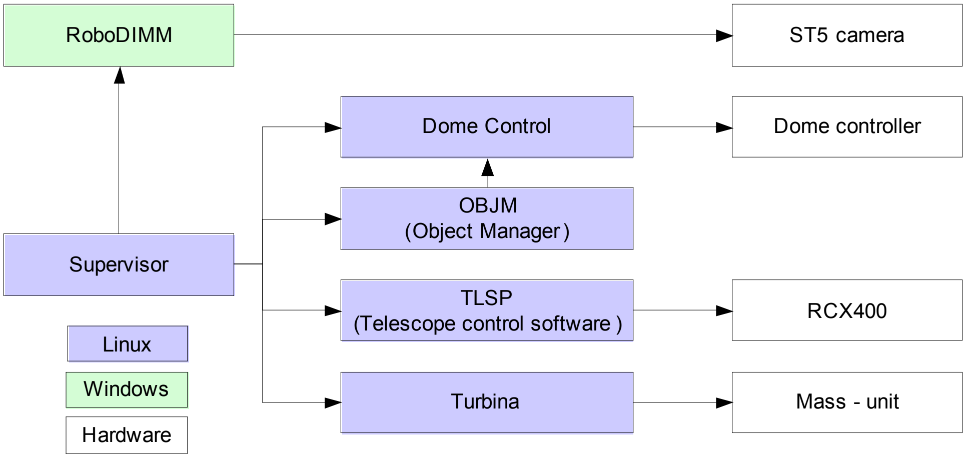

Fig. 2 Software block diagram

The remaining software is running on a Linux computer. The OBJM and TLSP software are running continuously in the background. The remaining software is controlled by a cron script:

@ 3 pm:	Turbina started (must be started before supervisor)
@ 4 pm:	Supervisor started
@ 7 am:	Turbina killed
@ 7.02 am:	MASS High Voltage is turned off (if the high voltage is on during daylight, the photon counters will be destroyed)
@ 10 am:	Supervisor killed

If high voltage is applied to the photon counters of the MASS instrument during daylight conditions, they will be destroyed. Therefore the high voltage is turned off every morning, in case the dome for some reason is opened during the daytime. This is a security measure, if the Supervisor program fails during the night run. Otherwise it will start and stop the measurements automatically when the Sun crosses a predefined angle below the horizon. Currently 10° is used.

A separate program is used to turn off the high voltage. This script requires that the Turbina software is stopped first. Restarting Turbina has the added benefit that a new data file is created every night. Otherwise the same data file would be used over several nights.

Both computers are connected to a NTP server to ensure correct time.

Software Configuration

Turbina requires a unique "device.cfg" file containing some device specific calibration parameters. Other than that Turbina and RoboDIMMnet requires information about geographic position and various calibration parameters dependent on the telescope optics described in the following section.

4. Calibration of the MASS-DIMM System

As described by Tokovinin (2005), it is necessary to carefully tilt and align the MASS-DIMM unit on the telescope to ensure the projected apertures at the front window telescope surface are not obscured by the telescope outer diameter, or its central obstruction. The pupil magnification and pixel scale can be calibrated by measuring the apparent diameter of each of the MASS diameters and the size and separation between the two DIMM apertures, and comparing them with the physical sizes of these apertures (Tokovinin, AT05, figure 3). This can be done by shining a light through each aperture, and drawing the projected images on a piece of paper held against the front window of the telescope. The back projected images should be sharp, otherwise the Fabry lens needs to be adjusted.

The projected DIMM aperture sizes for our system were measured to be 9.0 cm, and their separation is 21 cm. The CCD pixel size was measured to be 0.834 arcsec/pixel. The value described by Tokovinin (2005) of 0.85 arcsec/pixel was used.

For the MASS instrument, the magnification and focal length must be set. These depend on the optical system, i.e. telescope. The system magnification can be calculated based on the measured value of the back project MASS annulus diameters and the physical size of the segmentator diameters, which is supplied in the device dependent configuration file.

The two outer MASS apertures were measured to 9.0 and 6.1 cm. Calculating the magnification using the measured values for the segmentator, gives a magnification of 16.4 for the outer diameter, and slightly smaller for the second. Diameters of the two inner segments were not used, as the accuracy of the measurement was too poor. Thus we use a magnification value of 16.4, which happens to be the same value used in Tokovinin (2005).

Finally the noise of the photon counters was measured and the averaged value over 10 test runs was entered into the Turbina configuration file.

5. Algorithms

The DIMM instrument measures the summed Free + Boundary seeing. The data is stored in a file on the local DIMM computer. A new file is generated for each night.

The MASS instrument estimates the seeing at different heights, namely 0.5, 1, 2, 4, 8, and 16 km above ground level. The turbulence in the lower 0.5 km of the atmosphere, the so-called Boundary Layer, is not detected by the MASS instrument.

Both the MASS and DIMM data are measured and recorded approximately once every 90 seconds, but they are not synchronized and the interval between two measurements is not constant for either instrument.

The turbulence moment μ_m is defined by J. W. Hardy (1998):

$$\mu_m \equiv \int_0^\infty C_n^2(z) \cdot z^m dz$$

For the seven layer turbulence profile generated by the DIMM/MASS equipment, a discrete version of this equation is appropriate:

$$\mu_m \approx \sum_{i=0}^{6} C_n^2[i] \cdot z[i]^m$$

where z[i] = [0, 0.5, 1, 2, 4, 8, 16] (in km) for each of the 7 layers.

The MASS instrument measures $C_n^2[i]$ for $i = 1$ to 6 (for each of the 0.5, 1, 2, 4, 8, and 16 km layers) but does not detect the boundary layer $C_n^2[0]$. This can, however, be calculated from the DIMM data.

From J. W. Hardy (1998) we have:

$$Seeing = \frac{\lambda}{r_0} \quad (1)$$

and using R. J. Saiela (1994):

$$r_0^{-5/3} = 0.423 \cdot k_0^2 \cdot \mu_0 \quad (2)$$

where k_0 is the wavenumber:

the value of μ_0 can be calculated from the DIMM seeing data, and thus $C_n^2[0]$ can be calculated using:

(3)

The only remaining problem is that the DIMM and MASS measurements are not simultaneous in time. This is addressed by linear interpolation using two (DIMM-time, μ_0) data points to convert μ_0 into the MASS time frame. This value is then used in equation 3 to calculate $C_n^2[0]$, which is shown on a plot together with the 6 upper layers.

The Fried parameter r_0, shown in equation 2, is a measure of the lateral coherence scale of the wavefront phase. It can be calculated directly from the DIMM seeing data using equation ???, but in order to get the same time frame for the data, it is instead calculated using the linear interpolation of μ_0 and equation 2.

Wavefront aberrations de-correlate with increasing angular separation because light from stars in different directions on the sky traverse different turbulence columns through the atmosphere, meaning that wavefront aberrations de-correlate with increasing angular separation. Likewise the AO correction of wavefront phase aberrations for an on-axis star degrade for stars further away. The isoplanatic angle θ_0, is a measure of the angular correlation of the differential wavefront phase. θ_0 is calculated using R. J. Saiela (1994):

$$\theta_0^{-5/3} = 2.91 \cdot k_0^2 \mu_{5/3} = 2.91 \cdot k_0^2 \sum_{i=0}^{6} C_n^2[i] \cdot z[i]^{5/3}$$

which reduces to

$$\theta_0^{-5/3} = 2.91 \cdot k_0^2 \sum_{i=1}^{6} C_n^2[i] \cdot z[i]^{5/3}$$

because $z[0] = 0$ km. θ_0 can therefore be calculated directly from the MASS data.

An LGS-AO system uses back-scattered light from a laser to approximate the wavefront phase correction but, because of the finite height of the laser beacon, this correction differs from that for starlight: an effect called focal anisoplanatism. The lateral coherence scale parameter d_0 is a measure of the differential wavefront phase between the laser and star:

$$d_0^{-5/3} = k_0^2 \left(0.500 \frac{\mu_{5/3}}{H^{5/3}} - 0.452 \frac{\mu_2}{H^2} \right)$$

where H is the height of the laser beacon.

6. Webserver

The webserver retrieves the ASCII data files from the DIMM and MASS computers. The relevant data is extracted, and the algorithms described above are used to calculate the ground layer, r_0, θ_0, and d_0. These data are used to generate plots using GNUplot. The server retrieves data from both the MASS-DIMM instrument described here, and the TMT T5 MASS DIMM. Our scripts are written in Perl and run once per minute. The necessary webpages are dynamically updated whenever new data is available. The main page shows data from the last operating night for both systems. Another page shows graphs from the past 3 weeks and a third page provides links to all ASCII data and plots, which can be used by the observers for further processing.

7. Results

a. Turbulence Profiles and Parameters

A number of plots are generated and shown on the website. For the turbulence parameters, a reference wavelength of 500 nm is used, but for convenience is referred to on the plots as “V band”. The first plot shows the seeing measured by the DIMM and MASS instruments. Since the DIMM measures the summed Free + Boundary seeing and the MASS only measures the Free seeing, the value shown for the MASS instrument should not exceed the value shown by the DIMM instrument. However, lower level saturation effects may cause the free-atmosphere estimates to exceed the measured DIMM seeing.

The second plot shows the height resolved MASS measurements (for each of the nominal 0.5, 1, 2, 4, 8, and 16 km layers). In addition the ground layer profile (0 km) is calculated as described above. When the free-atmosphere seeing exceeds the DIMM seeing, the lowest layer in this figure is displayed as a negative value.

The Fried parameter is shown in the third plot. Large values of r_0 indicate that the wavefront is smooth, resulting in good image quality.

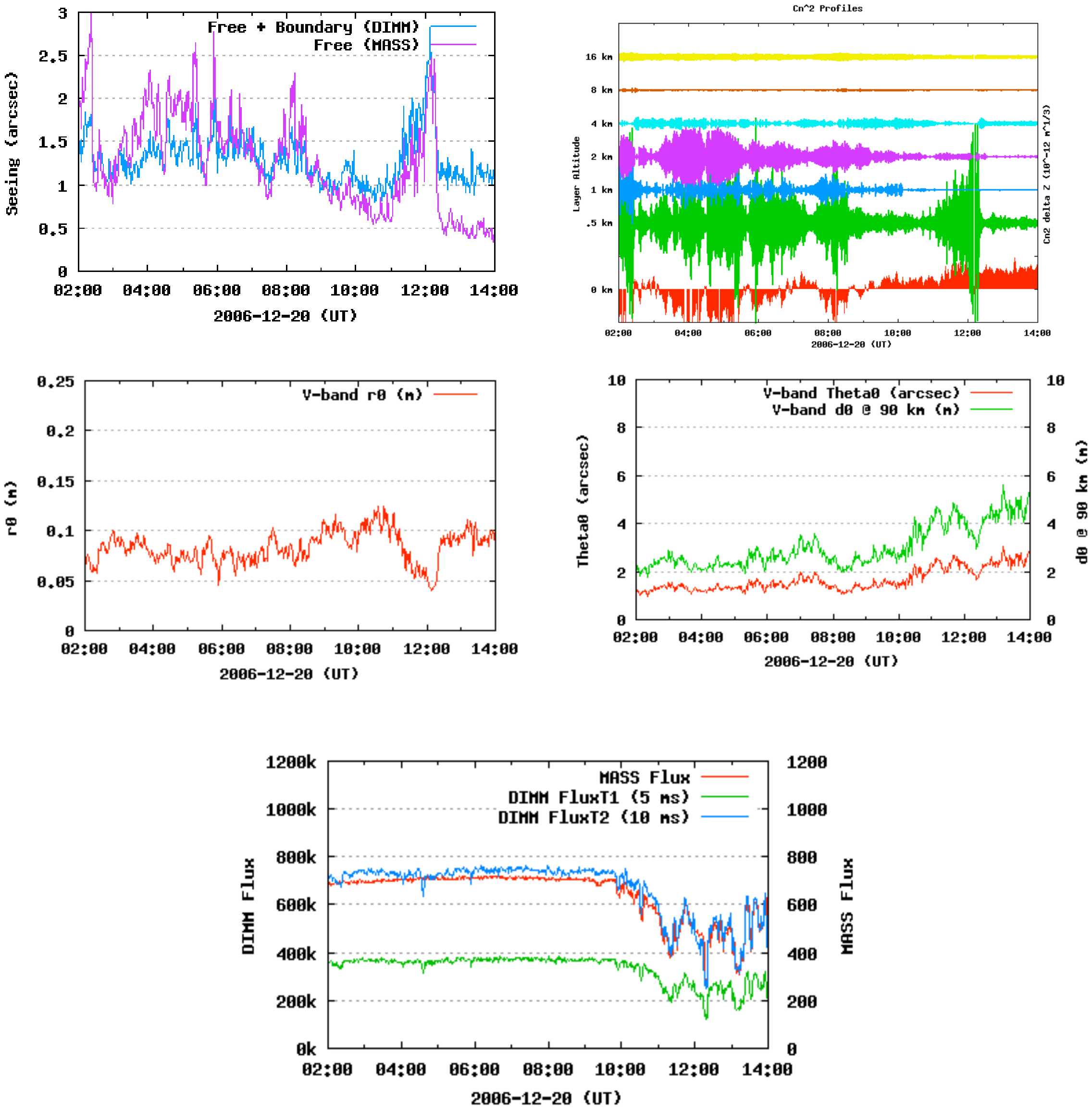

Fig. 3 Examples of the P18-MD data presented on the website. Each plot is described in the text

The fourth plot shows θ_0 and d_0. AO systems should deliver uniform image quality over fields of size θ_0, centred on the guide star, so large values of θ_0 indicate good image quality over large fields of view. For a laser guide star adaptive optics system, the wavefront phase differences are small near the center of the aperture, but grow as one moves out in the aperture plane. For apertures smaller than d_0, an AO system can deliver good image quality. For larger apertures, the differential phase aberrations become large at the outer edge of the aperture, resulting in little improvement in the image quality. In this sense, d_0 sets the effective size of the correctable aperture for a single laser guide star adaptive optics system. Large values of d_0 result in good image quality. The value of d_0 depends on the height of the laser beacon, and for these calculations a height of 90 km is assumed.

Note that the Fried parameter, r_0, the isoplanatic angle θ_0 and the focal anisoplanatism parameter d_0 all depend on wavelength to the $6/5^{\text{th}}$ power. The results presented in these plots are for 500 nm wavelengths. Longer observing wavelengths yield better image quality.

The final plot shows the atmospheric transparency computed from the raw counts measured using the DIMM and MASS instruments. The DIMM instrument captures images with alternating exposure times of 5 ms and 10 ms. Therefore two flux values are shown for the DIMM instrument. The flux estimate for the 10 ms DIMM image should be twice as high as the 5 ms DIMM image. A flux estimate from the MASS instrument is computed by summing the raw counts of the four channels. All three values should correlate, but have different magnitudes. Since the PMD is staring at Polaris, the airmass correction is constant.

b. T5/P18-MD Comparison

Turbulence profile measurements from the P18-MD unit may be compared to those from the T5 unit. Since these systems operate using different telescopes, this cross-comparison provides a consistency check, but since they are sited some 300 m apart local differences can occur. T5 sits on a concrete roof, is open to the atmosphere at night, but can suffer from local ground cooling effects in the evening. P18 is sited inside a dome with more wind protection. It is also important to note that T5 is tracking different stars during the night, whereas the P18-MD tracks Polaris all the time. This, and the difference in location and dome, will cause some difference in the measurements. So far we have only compared the DIMM dataset.

Since the two instruments sample independently it is necessary to somehow align the two datasets in time. We have chosen to do so in the following manner:

For each night, we run through all P18-MD DIMM data points. For each P18-MD DIMM data point the two nearest T5 data points (in time) are linearly interpolated to the time of the P18-MD measurement. If the two nearest T5 data points are more than 120 s away from the PMD data point, the data are discarded from the comparison. Normally T5 and PMD are sampling approximately every 90 seconds, so data are discarded only when observation on one of the instruments has stopped.

An alternative approach is to average all data points over a 6 minute interval. This has also been tried, and it gives the same trend as the method above, but obviously with fewer data points.

The data has been plotted in the following two figures. To the left T5 vs P18-MD DIMM seeing is plotted, and to the right the difference (T5 minus P18-MD) is plotted using the T5 data points as reference. These plots show that the P18-MD works up to a seeing of about 2.5 arcsec, above which the P18-MD does not capture the increased seeing. During operation we have also observed that the instrument when performing the spiral search during high seeing, has not recognized Polaris and skipped past it. This also explains why we get so few data points for the higher seeing values in the comparison.

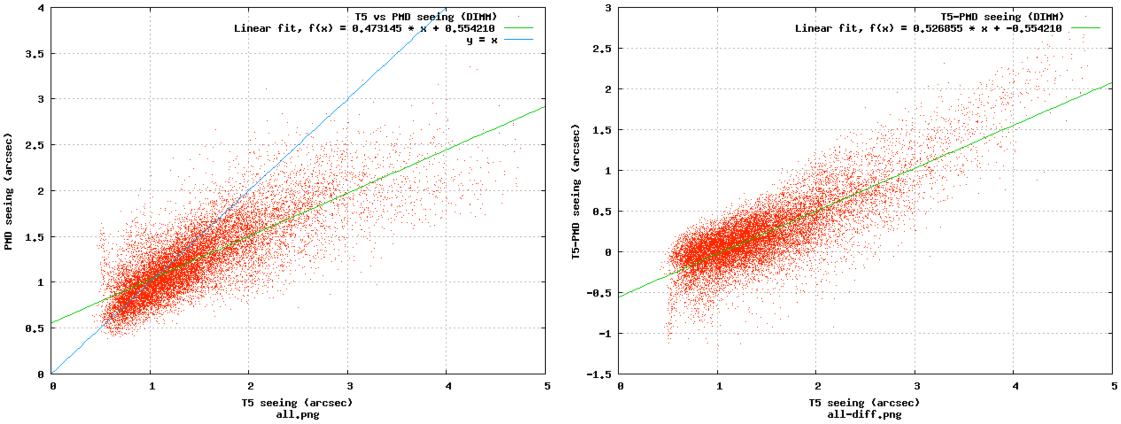

Fig. 4 Left: Comparison of P18 with T5 seeing results. Right: Difference (T5-P18) vs. T5 seeing

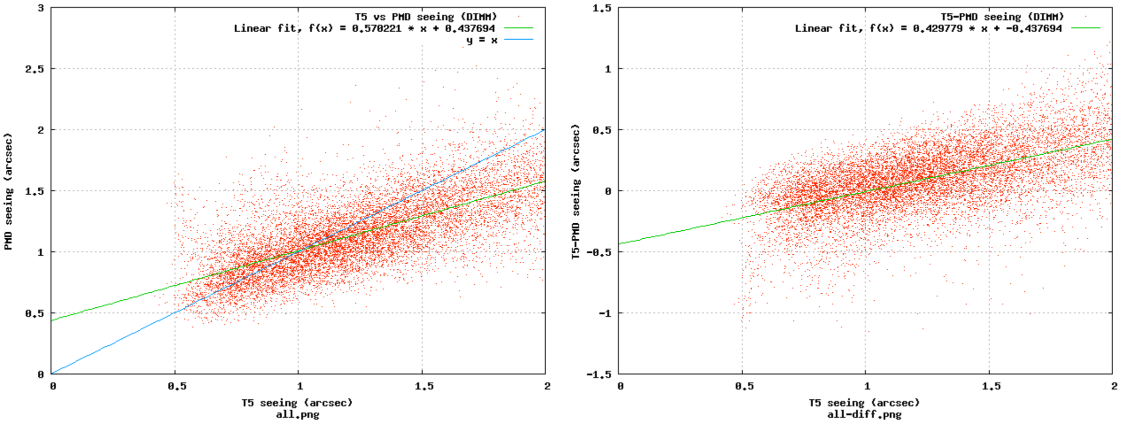

Fig. 5 As above for seeing values less than 2 arcsec

Figure 5 shows only the data for which the T5 measured a seeing of less than 2 arc seconds. The fitted line (green) shown in these plots includes only these data. The blue line shows the 1-to-1 relation. As can be seen from this figure, the fit for smaller seeing values is fairly good. Fortunately for image quality assessment the data obtained in better seeing conditions is of highest interest.

8. Implementation Status

The P18-MD unit was installed in September 2006. It has since been running every clear night, however it currently has some trouble finding Polaris during high seeing conditions. During normal operation, when the star has first been found tracking the star works really well, it is only lost when a cloud covers a star.

Sometimes the MASS instrument is overshooting the DIMM instrument. A new version of the Turbina software with improved data processing has been developed, but we have not yet installed it. Likewise the dome is still opened and closed manually, however an automatic system is being installed.

9. Conclusions and Future Work

We have described the MASS-DIMM system installed at Palomar in September 2006. The system is operating autonomously every clear night. The vertical turbulence profile along with derived parameters are stored in a database which is updated every minute. The data have been compared with another MASS-DIMM unit already operating at Palomar. The new DIMM instrument seems to have a problem during high turbulence, but it correlates well at seeing below about 2.5 arcsec. Fortunately for image quality assessment the data obtained in better seeing conditions is of highest interest. We are continuing to operate and experiment with the system to explore its predictive capabilities for: (i) Anisoplanatism comparison with LGS-AO observations, (ii) PSF fitting for narrow and wide field applications, (iii) input to GLAO measurements and (iv) site characterization.

References

A. Tokovinin, 2003: MASS-DIMM – a turbulence monitor for Adaptive Optics, http://www.eso.org/gen-fac/pubs/astclim/espas/workshops/AO-ATMO-2003/Tokovinin.pdf

A. Tokovinin, 2005: Matching MASS-DIMM to Meade RCX-400 telescope, Version 2, January 24, 2005, http://www.ctio.noao.edu/~atokovin/profiler/MD_RCX400.pdf

A. Tokovinin, 2006: Multi-Aperture Scintillation Sensor, http://www.ctio.noao.edu/~atokovinin/profiler/

J. W. Hardy, 1198: Adaptive Optics for Astronomical Telescopes, Oxford University Press

L. Wang, et al, 2006: High accuracy DIMM measurements for the TMT site testing program, SPIE 62671S

R. J. Sasiela, 1994: Electromagnetic Wave Propagation in Turbulence, Springer-Verlag

W. Skidmore et. al., 2004: The Thirty Meter Telescope site testing system, SPIE 5489, 154

The hybrid Shack-Hartmann/G-SCIDAR instrument

M. Ángeles C. Rodríguez-Hernández*, Jose M. Delgado, Jesús J. Fuensalida, Begoña García-Lorenzo, Elvio Hernández and Claudia Hoegemann
Instituto de Astrofísica de Canarias

ABSTRACT

We have built a hybrid turbulence profiler measuring simultaneously the atmospheric turbulence structure with a Shack-Hartmann wave front sensor and a G-SCIDAR (scintillation sensor). This is the first instrument combining two different techniques and measuring simultaneously the turbulence structure. The hybrid profiler has been installed at the Carlos Sanchez telescope at the Teide observatory. The G-SCIDAR arm is already working properly and we are still testing the Shack-Hartmann arm.

**Corresponding author address:* M. Ángeles C. Rodríguez-Hernández, Instituto de Astrofísica de Canarias
E-mail: ahernan@iac.es

LuSci: a simple lunar scintillometer to characterize ground layer seeing

Andrei Tokovinin,[*] Jayadev Rajagopal and Edison Bustos
Cerro Tololo Inter-American Observatory, La Serena, Chile

ABSTRACT

The contribution of the first 10-20m above ground to the total seeing may be significant and has to be measured in order to determine the height of future domes and to translate the site-testing data to higher domes. A simple yet accurate way to measure the C_n^2 profiles in the ground layer is offered by solar and lunar scintillation. We present a new simple lunar scintillometer, LuSci. A robust method of profile restoration including a model of lunar phases is developed. First tests of this technique are described.

---

[*] *Corresponding author address:* Andrei Tokovinin, Cerro Tololo Inter-American Observatory, Casilla 603, La Serena, Chile
E-mail: atokovinin@ctio.noao.edu

1. Why measure the GL turbulence?

Good seeing is beneficial for classical astronomical observations, but the location of turbulent layers producing the seeing is irrelevant. However, it is important to know how much turbulence is located in the first meters above the ground for determining optimum height of domes and for extrapolating the data of seeing monitors to the height of future domes. This is especially important for Antarctic sites where the ground layer (GL) is very strong, while the atmosphere above it is calm. New techniques such as adaptive optics (AO) require more or less detailed knowledge of turbulence profile. The intensity of turbulence in the GL determines the gain expected from ground-layer AO, while its thickness defines the size of the compensated field.

Classical method of GL studies with micro-thermal sensors is indirect and not cheap. On the other hand, weak scintillation produced by extended sources such as Sun and Moon can serve for direct optical sounding of GL turbulence. This idea was developed by Beckers (2001) and then used successfully for selecting a site of the solar telescope (Socas-Navarro et al. 2005). A lunar scintillometer has been tested by Hickson & Lanzetta (2004). Rapid detection of small ($\sim 10^{-4}$) scintillation presents some challenge in case of the Moon, while lunar phases must be accounted for in the data processing. We address these challenges by developing a simple lunar scintillometer, LuSci.

2. Profile restoration from Lunar scintillation

Scintillation of an extended source is fully described by geometric optics. It is achromatic and immune to saturation (Kaiser 2004). The covariance between normalized light fluctuations in two detectors separated by a baseline b is related to the turbulence profile $C_n^2(z)$ as

$$C(b) = \langle \frac{\Delta I_1}{I_1} \frac{\Delta I_2}{I_2} \rangle = \int W(z,b)\, C_n^2(z)\, \mathrm{d}z. \tag{1}$$

The *weighting function* $W(z,b)$ depends on the Moon's phase, detector size, and, for a large propagation distance z, on the turbulence outer scale L_0. An example of WFs is shown in Fig. 1.

A sharp cutoff is a characteristic feature of the WFs permitting to solve the inverse problem – to restore $C_n^2(z)$ from a set of covariances $C(b_i)$ measured on several baselines b_i. However, with only few detectors the number of baselines is small and restoration presents some problems, cf. Socas-Navarro et al. (2005).

We found such linear combinations of WFs that produce peaked response over certain intervals of z and are close to zero elsewhere (Fig. 1, right). This method gives turbulence intensity in thick "layers" with altitude resolution $\Delta z/z \sim 1$. The first two layers peaking at 4 m and 10 m are most useful for extrapolating the site-monitor seeing to the height of the telescope dome and for selecting this height.

Covariances resulting from the real Moon images at different phases were calculated. We found that an elliptical disk with suitably chosen diameters instead of a real Moon approximates these covariance to within 10% for the period of ±5 days around full Moon. Thus, we have a simple model for calculating the WFs that accounts for the Moon's phases.

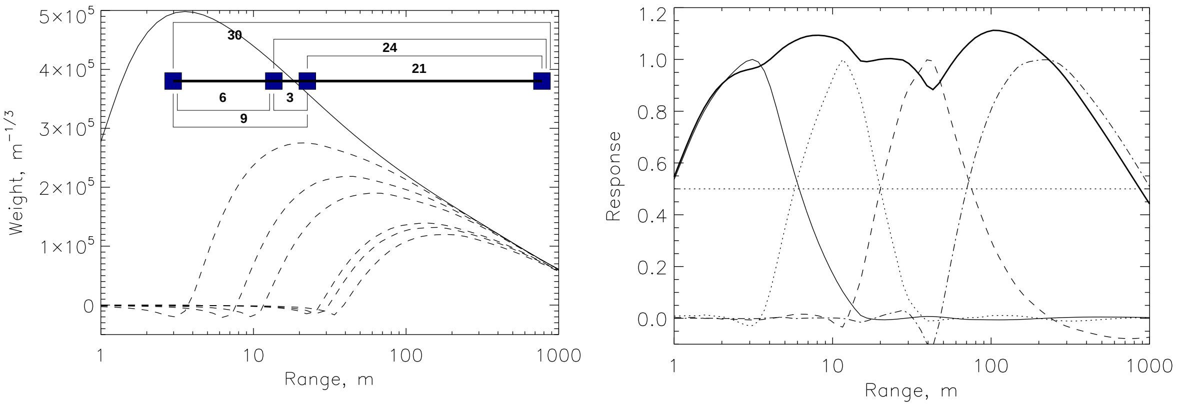

FIG. 1. Left: weighting functions $W(z,b)$ for the detector configuration 6-9-30 (baselines 0,3,6,9,21,24,30 cm). The full line shows autocorrelation, dashed lines – cross-correlations. Full Moon, 1-cm detector, turbulence outer scale $L_0 = 25$ m. Right: response functions resulting from suitable linear combinations of WFs, and their sum (upper envelope).

3. First tests of LuSci

We built a prototype LuSci instrument with four 1-cm square Si detectors. Their photo-current is amplified with a bandwidth of 0.5 kHz and digitized with 2-ms sampling by the commercial multi-channel acquisition module UDAQ 1600. The 16-bit resolution is insufficient to capture small fluctuations, hence the AC part of the signal above 0.1 Hz is additionally amplified and digitized separately. The intrinsic noise of the detector is less than the photon noise of the lunar flux (some $5.5\ 10^{11}$ photo-electrons per second from full Moon). We paid attention to shielding and grounding to avoid any pick-up noise.

The detectors are placed in a linear configuration with baselines (10, 13, 38) cm and their combinations. A rough blind restricts the field to $\pm 20°$, resulting in a $\sim$10% sky background relative to the Moon's flux (Fig. 2). The baseline is oriented along the polar axis, so that the whole device can be coarsely pointed to the Moon or diverted slightly for measuring the sky by rotating it along single axis.

LuSci worked at Cerro Tololo during several nights in February and March 2007. Figure 3 shows typical results over few hours. For comparison, simultaneous estimate of the GL seeing from the DIMM-MASS site monitor is plotted. The GL seeing measured by LuSci is not reduced to zenith, for this reason it is somewhat larger compared to the DIMM-MASS. Turbulence in the first few meters above ground was not strong, the dominating contribution to the GL seeing came from the layers above 55 m. On this night, the DIMM seeing measured at $h = 6$ m is representative of a seeing in a higher dome, and the dome height itself would have no effect because the layers at 12 m and 55 m contributed so little to the GL seeing.

4. Outlook

We explore the easiest and cheapest way to build a lunar scintillometer. Of necessity, the number of detectors is small and the vertical resolution of reconstructed turbulence profiles is not very high. Nevertheless, the results are already useful for evaluating the effect of the dome height

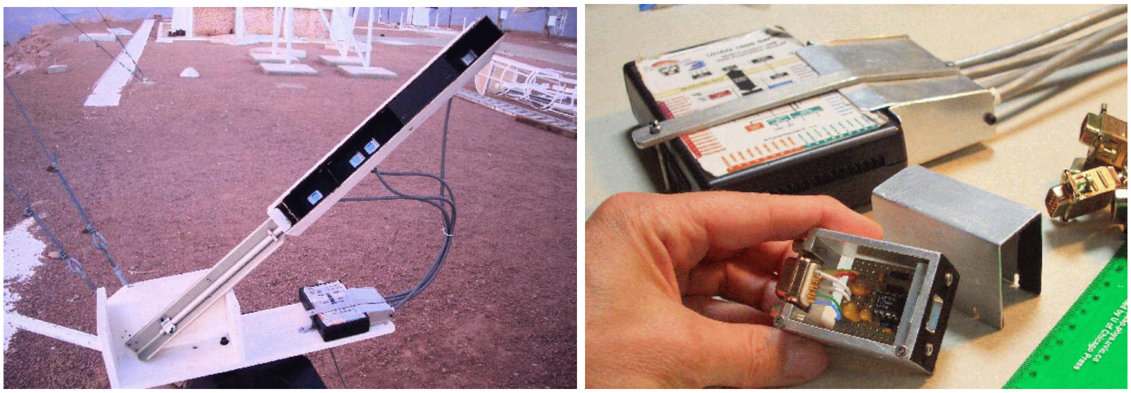

FIG. 2. Prototype LuSci instrument at Cerro Tololo (left) and its detectors (right).

on seeing. Alternative approaches to profile restoration will be applied to the same data, enhancing their usefulness and our confidence in the results. We plan to compensate for the small number of detectors by the analysis of the temporal correlation. If turbulence is moved in front of the single detector with a constant and known wind speed, the temporal correlation is a faithful representation of the spatial one and our set of baselines becomes virtually unlimited.

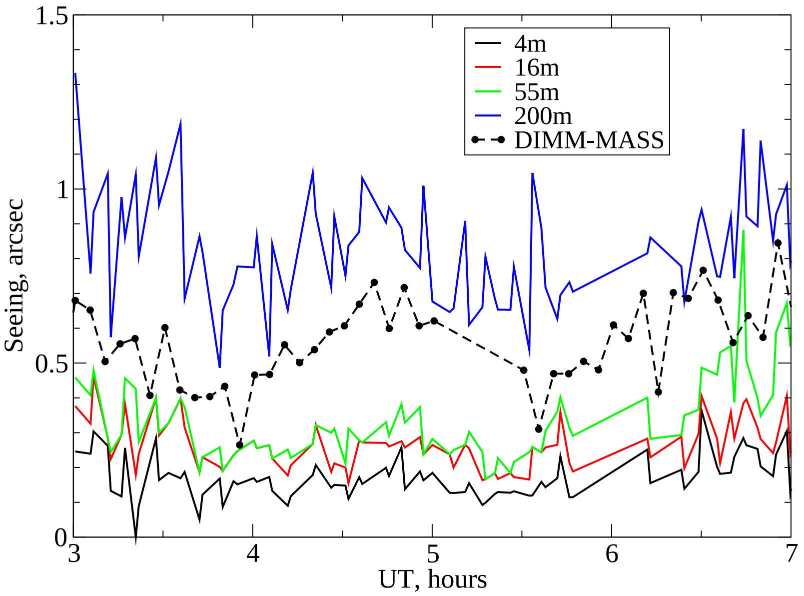

FIG. 3. Turbulence evolution in the ground layer at Cerro Tololo on March 6/7, 2007. Successive curves show GL seeing produced by the first layer at 4 m, two first layers, etc. For comparison, the GL seeing measured by DIMM-MASS is plotted.

References

Beckers, J. 2001, Exp. Astron., 12, 1

Hickson, P. & Lanzetta, K. 2004, PASP, 116, 1143

Kaiser, N. 2004, “Site evaluation using lunar shabar”. Pan-STARRS internal memo, http://pan-starrs.ifa.hawaii.edu/project/events/talks/2004-01-23_kaiser.pdf

Socas-Navarro, H., Beckers, J., Brandt, P., Briggs, J., Brown, T., Brown, W., Collados, M., Denker et al. 2005, PASP, 117, 1296

A G-SCIDAR instrument for the inter-calibration of the atmospheric turbulence between the Roque de los Muchachos and Paranal observatories

Jose M. Delgado*, Jesús J. Fuensalida, Begoña García-Lorenzo, Elvio Hernández,
M. Ángeles C. Rodríguez-Hernández and Marcios Reyes

Instituto de Astrofísica de Canarias

ABSTRACT

The most reliable and confirmed technique for measuring atmospheric turbulence profiles with height $C_n^2(h)$, is the well known G-Scidar method [Fuchs, Tallon & Vernin (1994)]. During the last 3 years, this technique has been implemented and developed with two automated instruments installed in the Roque de los Muchachos and in the Teide observatories. Periodic and continued measurements have been carried out for several years.

The installation and operation in Paranal Observatory (ESO, Chile) of a replica of these instruments has been included within the European Framework Program FP6 ELT Design Study, concretely into the WP12000 Site Characterization and WP 12200 Instrumentation, measurements and modelling work packages. This instrument has been adapted to the site infrastructure.

This G-Scidar instrumentation has been developed under the standard requirements of measurement techniques, acquisition procedures and methods of analysis established into the WP12000. It will permit the suitable automatic control and position of the devices, with near performances of real-time measurements. In addition, it should allow reliable inter-calibration of data obtained at the different sites.

The basic concept of the instruments and their features are described, detailing the adaptability peculiarities of each one to the different telescopes which support them. Furthermore, the specific characteristics of automatic reduction procedures are shown as well.

**Corresponding author address:* Jose M. Delgado, Instituto de Astrofísica de Canarias
E-mail: jdelgado@iac.es

From the simulated annealing method to Single Star Scidar

Zouhair Benkhaldoun* and Habib Abdelfetah

Laboratoire de Physique des Hautes Energies et Astrophysique
Cadi Ayyad University, Marrakech

ABSTRACT

Optical remote sensing of atmospheric turbulence allows us to get information about the optical quality of atmosphere. A new procedure that we use to obtain atmospheric turbulence profile is based on the simulated annealing principle. Optical remote sensing of atmospheric turbulence allows us to get information about the optical quality of atmosphere. A new procedure that we use to obtain atmospheric turbulence profile is based on the simulated annealing principle. This method allows us to retrieve, for each turbulent layer, the altitude, the integrated value of the refractive-index structure coefficient over the thickness of the turbulent layer, the horizontal wind speed and the standard deviation of the horizontal wind speed fluctuations. These atmospheric parameters are extracted from the spatial-temporal cross-correlation of a single star scintillation (Single Star SCIDAR). The temporal sampling, which depends on the camera and computer features, is one profile every 11.2 seconds. Thus, it is possible to get the seeing and other parameters for adaptive optics with the same temporal sampling. This technique has allowed us to bring to reality the mobile SCIDAR system using a small telescope diameter, which is a useful means for site testing. These atmospheric parameters are extracted from the spatial-temporal cross-correlation of a single star scintillation (Single Star SCIDAR). The temporal sampling, which depends on the camera and computer features, is one profile every 11.2 seconds. Thus, it is possible to get the seeing and other parameters for adaptive optics with the same temporal sampling. This technique has allowed us to bring to reality the mobile SCIDAR system using a small telescope diameter, which is a useful means for site testing.

**Corresponding author address:* Zouhair Benkhaldoun, LPHEA, Cadi Ayyad University, Marrakech.
E-mail: zouhair@ucam.ac.ma

Generalized and High-Vertical-Resolution SCIDAR measurements at Mt. Graham

Sebastian Egner*
Max Planck Institute for Astronomy, Heidelberg, Germany

Elena Masciadri
Osservatorio Astrofisico di Arcetri, Florence, Italy

Dan McKenna
Steward Observatory, Tucson, Arizona

ABSTRACT

We present the results of Generalized SCIDAR (GS) measurements of the vertical distribution of the optical turbulence above Mt. Graham in south-eastern Arizona. First results of an on-going site-characterization campaign covering 16 nights, distributed over 1 year are presented. The measured C_N^2 profiles show that most of the turbulence above Mt. Graham is concentrated near the ground and that Mt. Graham is excellently suited for astronomical observations in terms of seeing, isoplanatic angle and coherence time. A fine sampling of the complete atmospheric turbulence can be achieved by combining the data from GS analyzed in conventional fashion with a vertical resolution of $\approx$1 km and those obtained with a newly developed method, based on GS, with a vertical resolution of $\approx$25 m in the first 1500 m above the ground. Moreover, the impact of the retrieved turbulence profiles on Adaptive Optics systems, in particular, the optimal conjugated heights of the Deformable Mirrors optimized for narrow as well as large FOVs, are estimated.

---

*Corresponding author address: Sebastian Egner, Max Planck Institute for Astronomy, Koenigstuhl 17, 69117 Heidelberg, Germany.
E-mail: egner@mpia.de

1. Introduction

The LBT (Large Binocular Telescope) is currently being commissioned at Mt. Graham and will make use of sophisticated AO and MCAO systems. In order to optimize the design of these AO system and to achieve the best possible performance, it is essential to know the turbulence characteristics above the telescope. For these reasons, a dedicated site-characterization campaign with a SCIDAR instrument mounted to the VATT to measure the atmospheric turbulence above Mt. Graham is currently being performed.

2. Observations

So far we have measured ≈10 000 C_N^2 profiles, distributed over 16 nights in 2004 and 2005. We furthermore determined the wind speed profiles and the dome-seeing from the measured cross-correlation images as described in Avila et al. (2004). The median profiles for each night and for all the data have been calculated and are shown in figure 1. From the measured C_N^2 and wind speed profiles, the astro-climatic parameters, such as seeing ϵ_0, isoplanatic angle ϑ_0, wavefront coherence time τ_0 and isopistonic angle ϑ_P, are calculated (figure 2). With proper subtraction of the dome-seeing, we obtained median values for ϵ_0 (0.67 arcsec), ϑ_0 (2.7 arcsec), τ_0 (3.6 msec) and ϑ_P (3.3 arcsec). A more detailed analysis can be found in Egner et al. (2006b, 2007).

3. High-Vertical-Resolution SCIDAR

The vertical resolution for conventional Generalized SCIDAR is limited by the scintillation effect to ≈1 km at the ground (Prieur et al. 2001) (figure 1). For each layer, the FWHM of the associated peak in the auto-correlation images corresponds to a vertical range of ≈1 km (figure 3). This means that if the distance between two turbulent layers is smaller, their respective correlation peaks overlap, and the layers cannot be separated anymore. However, for MCAO systems, which correct single layers, it would be highly desirable to obtain C_N^2 profiles with a higher vertical resolution. To achieve optimal performance, it is essential to know the location and the strength of these layers and especially the inner structure of the ground layer, which usually contains most of

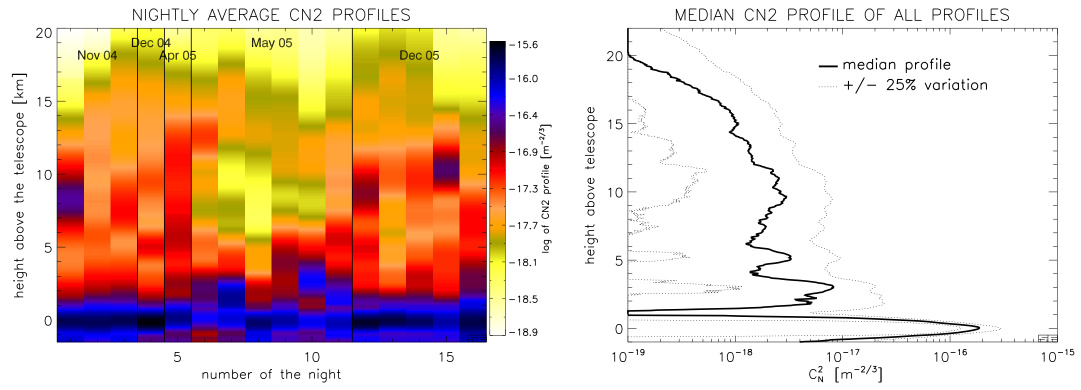

FIG. 1. **Left:** The mean C_N^2-profiles for all nights. The dome-seeing is removed and the C_N^2 intensity is plotted color-coded in logarithmic scale with yellow denoting weak, and blue strong turbulence. **Right:** The median C_N^2-profile (solid line) calculated from all measured data after subtraction of the dome-seeing and ±25% deviation.

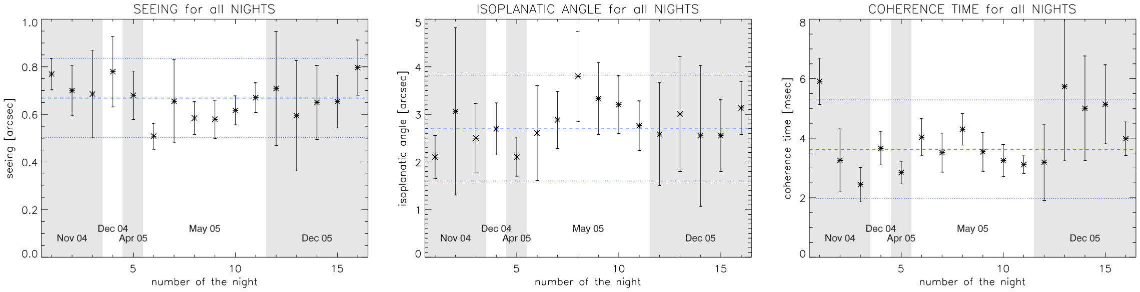

FIG. 2. **Left:** The median seeing ϵ_0 for the individual nights. The error bars represent the standard deviation of the respective variations during the single nights. The dashed lines indicate the median value and the dotted lines enclose one standard deviation with respect to all C_N^2-profiles. **Middle:** The median value of the isoplanatic angle ϑ_0 for all nights. **Right:** The median value of the wavefront coherence time τ_0 for the individual nights.

the turbulence (figure 1).

If the peaks in the correlation frames corresponding to different turbulent layers could be somehow separated, the vertical resolution might be improved. Such a possibility is given for the cross-correlation images (figure 3), where the correlation peaks are additionally shifted according to the wind speed in the corresponding turbulent layer. The idea is therefore to use the temporal cross-correlation images instead of the auto-correlation images to determine the C_N^2 profile (Egner et al. 2006a). Figure 4 shows the results obtained with this new method for a typical night.

4. Optimal conjugated heights for DMs in MCAO

LINC-NIRVANA (Gaessler et al. 2005) is a Fizeau interferometer currently being developed for the LBT. It will use a MCAO system with two deformable mirrors (DMs), where the conjugation height of the high-layer DM can be freely adjusted. To calculate the optimal conjugated heights of the DMs, we used a semi-analytic model (Egner et al. 2006b; Jolissaint and Veran 2002; Owner-Petersen and Gontcharov 2002) to calculate a filtered C_N^2 profile after correction by the MCAO system. From this residual C_N^2 profile, the Fried parameter r_0 (and thus the Strehl ratio on-axis) and the isoplanatic angle ϑ_0 can be calculated. The optimal height of the DM is then given by the altitude for which the Strehl / isoplanatic angle is maximal. The optimal conjugated heights of the high-layer DM for the individual nights is shown for the two cases in figure 5.

5. Conclusion

We presented the results of 16 nights of observations with a SCIDAR at the VATT on Mt. Graham. The retrieved astroclimatic parameters are comparable to other good astronomical sites, the optimal conjugated height for the high-layer DM when using the criteria for highest Strehl is ≈3.3 km and for the isoplanatic angle ≈11.1 km. However, more data is required to confirm the observed seasonal trends in the vertical structure of the turbulence. Further GS runs at Mt. Graham are planned as part of the FOROT Project activities.

Furthermore, a new method was presented to retrieve C_N^2 profiles with a high vertical resolution of ≈25 m in the first 1 500 m above the telescope. It is based on the analysis of temporal cross-correlation images of the scintillation pattern in the telescope pupil as measured with a Generalized

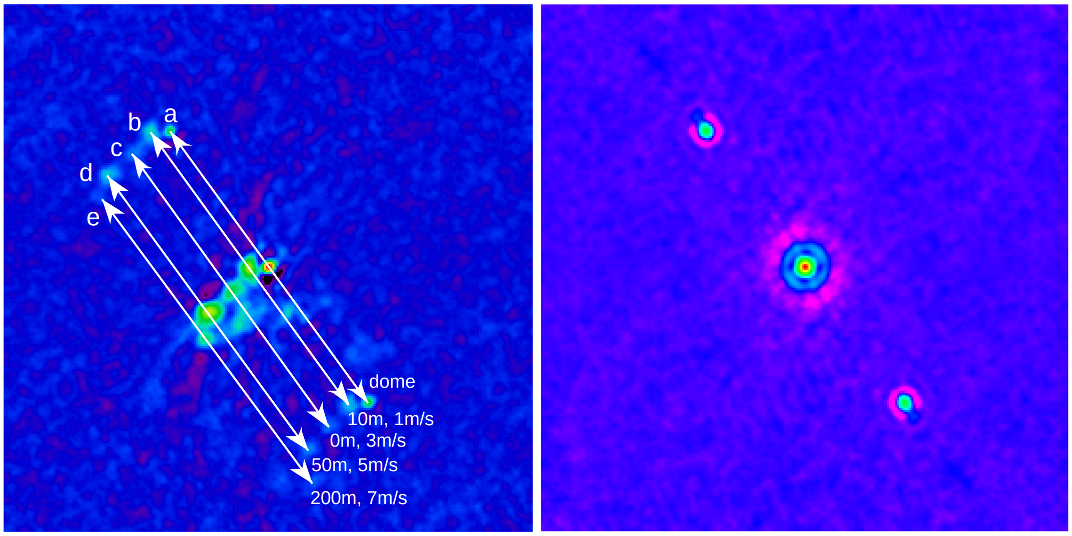

FIG. 3. A sample of a cross- and auto-correlation image, measured for a binary with 35 arcsec separation to illustrate the principle of the HVR-GS method. In the cross-correlation image (**left**), each turbulent layer produces a “triplet” (a central and two lateral peaks). The shift of the central peak is related to the wind speed in that layer and the separation of the two lateral peaks corresponds to the height of the layer above the telescope. In such a case, layers which are close together in altitude, but have a different wind speed ($\Delta v \approx$0.5 m/s) can still be separated. This is contrary to the auto-correlation image (**right**), where the single peaks overlap to form only one correlation peak. For the HVR method, the height of the layer is calculated from the separation of the lateral peaks (can be done with a precision of 25 m) and the C_N^2 value from the intensity of the central peak in the cross-correlation image. The retrieved heights above the telescope and the wind speeds are indicated tor the detected triplets.

SCIDAR instrument and on using a wide binary star (≈35 arcsec separation). With this vertical resolution, the inner structure of the ground-layer can be resolved, showing a variety of layers, with the strongest turbulent layer located at ≈50 m above the telescope. Half of the total turbulence in the atmosphere was found to be located within ≈170 m above the ground. This concentration of the turbulence very close the ground underlines the sensitivity of the achievable image quality on the actual position of the telescope on the mountain.

Acknowledgments.

The work was funded by the Alexander von Humboldt Foundation through the Wolfgang Paul Prize. E. Masciadri is funded by a Marie Curie Excellence Grant (FOROT), MEXT-CT-2005-023878.

Based on observations with the VATT: the Alice P. Lennon Telescope and the Thomas J. Bannan Astrophysics Facility. We thank Richard Boyle for his kind support at the VATT and the MGIO facilities to make our observations possible.

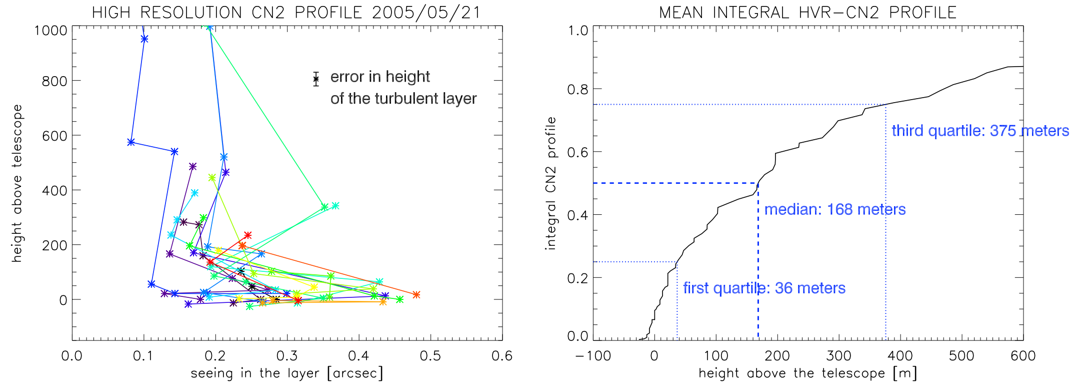

FIG. 4. **Left:** The seeing in single layers as retrieved from the data of 21 May 2005 with the high-vertical resolution SCIDAR method. Each color corresponds to one HVR-GS $C_N^2(h)$ profile. The vertical resolution is ≈25 m (as indicated by the error bar). A weak layer is located just outside the dome, but the strongest layer is for most of the time at around 50 m above the telescope, and another layer at ≈350 m. **Right:** The cumulative C_N^2 profile, which is a measure for the total amount of turbulence below a given altitude, as determined by combining the conventional Generalized SCIDAR and the high-vertical resolution SCIDAR (HVR-GS) technique. Half of the total atmospheric turbulence is below 168 m above the ground.

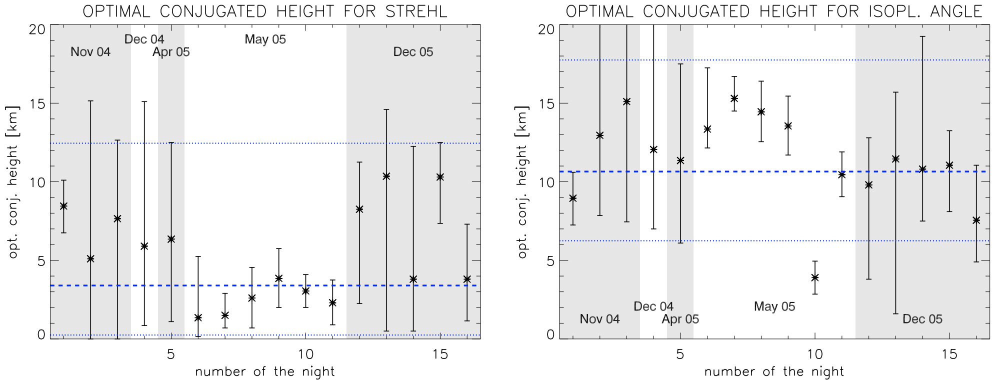

FIG. 5. The optimal conjugated height above the telescope of the high-layer DM of LINC-NIRVANA in the case of highest Strehl ratio on-axis (**left**) and in the case for largest isoplanatic angle (**right**). For optimal Strehl ratio it is important to correct the strongest layers (which are close to the ground, figure 1), whereas for large isoplanatic angle the turbulent layers at high altitude have to be corrected. For both criteria there is a significant seasonal variation apparent. Due to the strong turbulence in the ground-layer, the ground-layer DM should be always conjugated to ≈100 m above the ground.

References

Avila, R., E. Masciadri, J. Vernin, and J. Sánchez, 2004: Generalized SCIDAR Measurements at San Pedro Mártir. I. Turbulence Profile Statistics. *PASP*, **116**, 682.

Egner, S., E. Masciadri, and D. McKenna, 2007: Generalized SCIDAR measurements at Mt. Graham. *PASP*, accepted for June 2007 issue.

Egner, S., E. Mascidari, D. McKenna, and T. Herbst, 2006a: Beyond conventional G-SCIDAR: the ground-layer in high vertical resolution. *SPIE*, 6272.

Egner, S., E. Mascidari, D. McKenna, T. M. Herbst, and W. Gaessler, 2006b: G-SCIDAR measurements on Mt. Graham: recent results. *SPIE*, 6272.

Gaessler, W., C. Arcidiacono, S. Egner, T. Herbst, D. Andersen, H. Baumeister, P. Bizenberger, H. Boehnhardt, F. Briegel, M. Kuerster, W. Laun, L. Mohr, B. Grimm, H.-W. Rix, R.-R. Rohloff, R. Soci, C. Storz, W. Xu, R. Ragazzoni, P. Salinari, E. Diolaiti, J. Farinato, M. Carbillet, L. Schreiber, A. Eckart, T. Betram, C. Straubmeier, Y. Wang, L. Zealouk, G. Weigelt, U. Beckmann, J. Behrend, T. Driebe, M. Heininger, K.-H. Hofmann, E. Nussbaum, D. Schertel, and E. Masciadri, 2005: LINC-NIRVANA: MCAO toward Extremely Large Telescopes. **6**, 1129.

Jolissaint, L. and J.-P. Veran, 2002: Fast computation and morphologic interpretation of the Adaptive Optics Point Spread Function. *BCAO*, 201.

Owner-Petersen, M. and A. Gontcharov, 2002: Multi-conjugate Adaptive Optics for Large Telescopes Analytical Control of the Mirror Shapes. *JOSA*, **19**, 537.

Prieur, J.-L., G. Daigne, and R. Avila, 2001: SCIDAR measurements at Pic du Midi. *A&A*, **371**, 366.

Some observing campaigns with Single Star SCIDAR

Habib Abdelfetah* and Zouhair Benkhaldoun
Laboratoire de Physique des Hautes Energies et Astrophysique
Cadi Ayyad University, Marrakech

ABSTRACT

Using the Single Star SCIDAR system and the Simulated Annealing technique, we have analysed observation data obtained during three observing campaigns. The experiment was performed with three different telescopes of diameters : 152-cm and 80-cm at the Observatoire de Haute Provence (OHP) and a 63-cm telescope at Observatoire de SIRENNE in France. We note that the simulated annealing technique is a new method to retrieve the atmospheric turbulence profile.

The data obtained are the spatio-temporal cross-correlations of a single star scintillation. Using the simulated annealing method we can obtain the profile of the integrated value of the refractive-index structure coefficient, the horizontal wind speed and the standard deviation of the horizontal wind speed fluctuations. From these profiles we can get the temporal evolution of the seeing, the isoplanatic angle, and the coherent time of wave-front. The temporal evolution is one profile every 11.2 s. It is also possible to have the telescope dome seeing.

Corresponding author address: Benkhaldoun Zouhair, LPHEA, Cadi Ayyad University, Marrakech.
E-mail: zouhair@ucam.ac.ma

SITE TESTING IN THE NORTHWEST OF ARGENTINA

Pablo Recabarren (1,2,5), Diego García Lambas (1,2), Hernán Muriel1,(2), Federico Stasyszyn (1), Victor Renzi (1), Ruben Vrech (1), José Viramonte (2,4) and Marc Sarazin (3).

(1) *IATE-Observatorio Astronómico de Córdoba, Argentina.* (2) *CONICET, Argentina.* (3) *ESO, Germany.* (4) *Instituto Geonorte-UNS, Argentina. (5) Facultad de Ciencias Exactas, Fisicas y Naturales, U.N.Cba., Argentina.*

Abstract:

We present different results of the characterization of the Tolar Grande - Macon Range site in the North-West of Argentina. This project is being developed by the IATE Group of Córdoba Observatory in collaboration with ESO in the framework of the E-ELT project. We present and discuss one year of image quality measurements with MASS and DIMM, three years of meteorological data and detailed studies of seismic activity and geo-technical aspects as well as diverse logistic issues.

Geographic description

The NW of Argentina between, 23º 15' and 24º 30' South latitude and 65º 30' and 67º 30' West longitude, Known as Puna region, is a high plateau ranging between 3000 and 4000 m. There are several mountain ranges with peaks reaching more than 6000 m.

General facilities of the area

Salta is the main city, comparable or larger than the Chilean Calama and Antofagasta. Salta provides facilities and infrastructure such as airports, universities, communications, electric power stations, hotels, car and truck rentals, shopping centers, etc.

San Antonio de los Cobres: is the main town of our interest area (3781 m.a.s.l., 3200 inhabitants) through a 120 km paved road from Salta.

Tolar Grande: Small town of 175 inhabitants (3550 m.a.s.l) close to the site: Macón Range 320 km away from Salta (200 from San Antonio de los Cobres through a non paved road in good conditions. *A railway track from Salta City to Antofagasta (Chile) through San Antonio de los Cobres, Tolar Grande and Socompa pass.*

The Candidate Site (Macón Range)

Four candidate locations were preliminary selected after GOES satellite images, NIMBUS data analysis, analysis of tectonic and geographical issues as well as several exploration trips to the area. Macón Range: Toward the East of Arizaro Salt Flat, there is the Macon Range, at 5450 m.a.s.l. extends from the southeast of Mount Rincon, in the Chilean border to the South East of Tolar Grande Town, at the East of the middle of Arizaro salt flat. Macon Range runs in north to south direction and there are no comparable altitudes to the west near 50 km.

Macón range has several features that make it suitable for large observational developments. The combined facts of wind regularly from the WNW and E directions, the North- South layout of the Macon range and the presence of the large Arizaro Salt Flat at the West of Macón and Pocitos Salt flat at the East, provides particular configuration that strongly suggest a laminar wind regime on the top of the ridge.

Tolar Grande (which offers several facilities) is located between the Macon Range and the Arizaro Salt Flat.

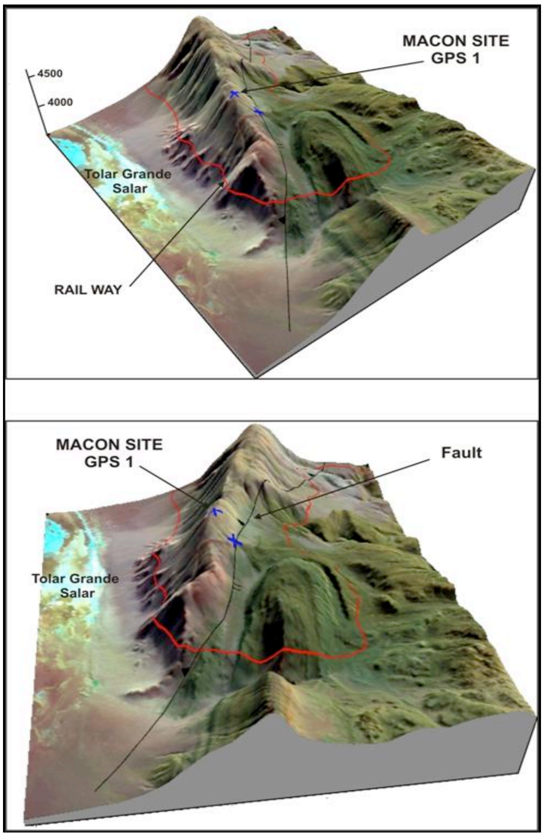

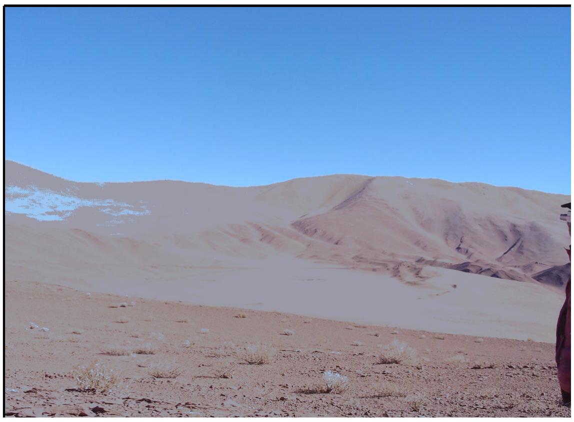

Left: Macón Range (the red line represents the railway track. Right: View of Macón site from the east.

Cloud Covering & Extinction
GOES 8 images from years 1999 to 2002, were analysed. The cloud covering distribution at local time 21, 00, 03 and 06 hs. (Local Time = UTC + 3hs.) indicates that approximately 83 % of night time is cloud free. During the 2 year campaigns in Tolar Grande it was observed clear sky during more than 90% of the time. Clouds disturbed MASS operation in 6 nights out of 152. Nimbus-7 TOMS satellite data indicates thet the region is not affected by dust, with extinction estimates better than those derived for Chajnantor plateau.

Light Pollution
Light pollution is negligible in the area of interest and it is not expected to change significantly in decades.

Meteorological results
Weather parameters are obtained every each 10 minutes, since January 2004.

Water Vapor
Atmospheric Opacity at 210GHz (Instituto Argentino de Radioastronomía). Results correspond to one year of measurements (April 2004 to April 2005).

Geological and Geotechnological Characteristics
The Cerro Macón granitoid is part of the Basement of the Puna. Considering the characteristics of the rock (Fresh granitic rock with diaclases) the admissible tension is around 35 kg/cm2.
The recent detritical cover is very poor or inexistent. The microscopic and chemical analysis of this sediment shows no presence of salt crystals and does not detect the

presence of SO4, in consequence they consider the soil is not aggressive to the cement. The granitic clast on Macon does not show a typical desert pavement or ventifact form. The absence of eolic sedimentary deposits, salt minerals and desert pavement and ventifact forms at the top of Macón, suggests that the wind do not have the possibility of transporting sedimentary material from the Arisaro salt flat.

Seismic Activity

The seismicity in the Puna Plateau is quite different than the one of the forearc region, being the later closer to the subduction trench of the Nazca Plate below the South American Plate. The west mountain range acts like an effective dumper of the seismic waves, especially to the secondary ones. There is a low superficial seismicity. Mostly the seismicity is owed to the subduction phenomena, so the focuses have depths of more than 100 km. The seismic hazard is defined in terms of peak accelerations: the peak acceleration is 0.19 g. The study gives quite lower values of the seismic loads than those of the forearc region.

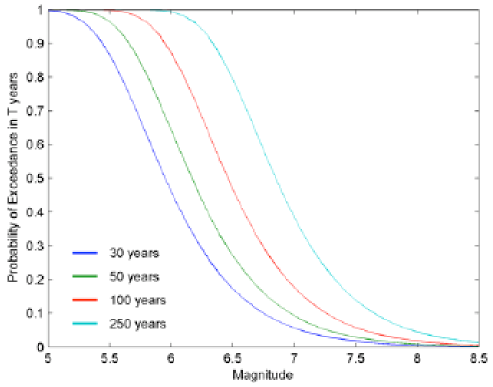

Figure 9. Rate of exceedance of body magnitudes for the seismogenetic zone I

Seeing and turbulence measurements

Measurements were obtained in the two sites: Tolar Grande Town 3550 m.a.s.l. and Macon ridge, 4609 m.a.s.l. In Tolar Grande, turbulence profiles were determined with ESO-MASS. In Macon ridge, weather parameters and atmospheric opacity at 210 HGz were also determined. Seeing measurements are obtained with the ESO-DIMM._Six MASS campaigns were performed covering the period 3/10/2005 – 4/28/2006, comprising 158 nights.

Five DIMM measurement campaigns in Macon range were developed simultaneously to MASS measurements in Tolar Grande village. We obtained 30 nights of DIMM measurements in the period 5/30/2005 – 4/28/2006.

Seeing and turbulence main results

DIMM seeing in Macón:

Mean = 0.70, Median = 0.55. (Paranal during the same days: Mean = 1.03, Median = 0.82).

DIMM seeing in Macón (4609 m.a.s.l.) vs. MASS seeing in Tolar Grande (3550 m.a.s.l.): The results indicates similar distribution of values. Nevertheless, MASS tends to underestimate DIMM measurements at Macón.

MASS at Tolar Grande: Free seeing : Mean = 0.61, Median = 0.52

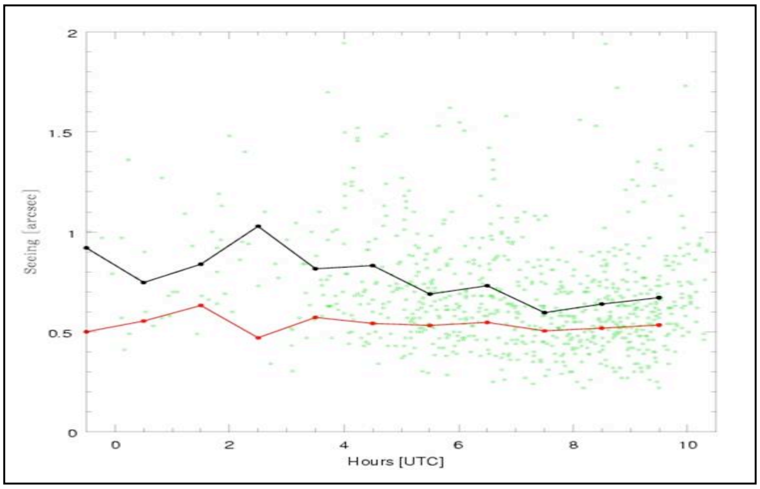

DIMM at Macón. Read: median values, Black: mean values.

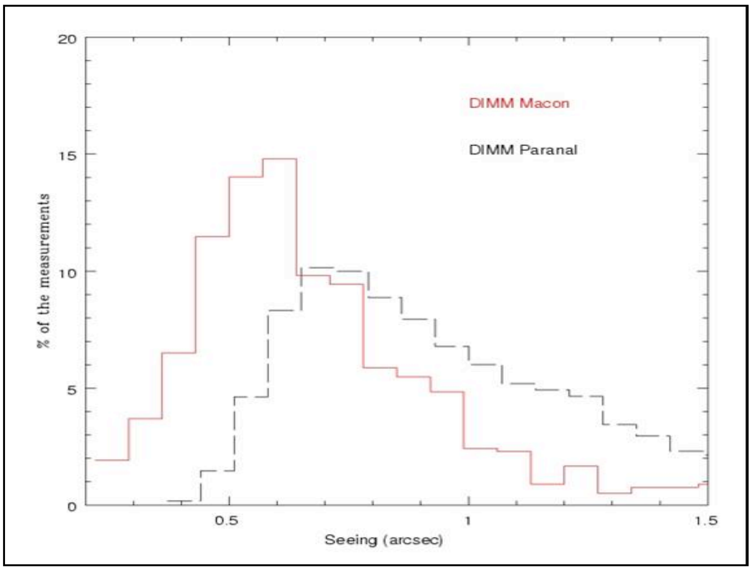

DIMM Macón vs. DIMM Paranal for the same days.

The Next Step
New Equipment and measurements

- C11 carbon fiber telescope.
- Robotic mount.
- MASS-DIMM instrument.
- 5m Tower & robotic enclosure.
- New meteorological weather station.
- Equipped container for human occupation.
- Access road to candidate site (12 km).
- MASS-DIMM measurements will be taken continuously in the Macón Range at 4650 m during a period of (at least) 12 months.

The Past, Present, and Future of Site Testing for the Southern African Large Telescope

Steven M. Crawford*
South African Astronomical Observatory, Cape Town, South Africa

Andrew Sheinis
University of Wisconsin, Madison, Wisconsin

ABSTRACT

The Southern African Large Telescope (SALT) is an 11m segmented telescope located in Sutherland, South Africa. The design of the telescope, with a primary consisting of 92 1-meter spherical segments, allows for both traditional adaptive optics systems along with the design and implementation of unique systems. Assessing the quality and stability of the Sutherland site is required to understand the feasibility of any future adaptive optics designs and producing effective and economical AO systems. In this contribution, we review the history of the Sutherland site, current measurements of the conditions recorded since the initial operations of SALT, and future measurements of the atmospheric conditions at SALT. Potential future measurements include combined MASS/DIMM measurements of the integrated seeing at different heights and detailed analysis of the micro-environment associated with the structure.

---

*Corresponding author address: Steven M. Crawford, South African Astronomical Observatory, Observatory, 7935 Cape Town, South Africa
E-mail: crawford@saao.ac.za

1. Introduction

Astronomical operations of the South African Astronomical Observatory (SAAO) were relocated in 1972 to a remote, dark site in central South Africa. The Sutherland Observing Station centralized the resources of SAAO in a site with stable year round weather with very dry conditions, making the site ideal for near infrared observations (Buckley et al. 2005). In 2000, ground breaking began on the Southern African Large Telescope (SALT), an 11m telescope based on an design of the Hobby-Ebberly Telescope. The improved design allowed for the construction of a powerful, yet cost efficient telescope. First light instruments for SALT include an imaging and acquisition camera (SALTICAM) and a prime focus mutli-mode spectrograph (Robert Stobie Spectrograph, RSS). Planned second generation instruments include a NIR upgrade to the RSS and a high resolution fiber-fed spectrograph.

SALT was primarily designed as a spectroscopic telescope, and moderate improvements in the seeing through low level adaptive optics can result in significant gains in throughput and resolution. However, the atmospheric behavior at Sutherland, where SALT is located, is not well constrained. In this contribution, we review the history of site testing at the Sutherland site as well as the current plans to measure the atmospheric conditions. Assessing the feasibility of any future adaptive optics (AO) system will depend on an accurate profile of the atmospheric turbulence.

2. Past and Present Site Testing at Sutherland

Prior to the construction of SALT, a significant campaign was undertaken to determine the best site at Sutherland for the telescope. An early study by Gochermann et al. (1998) during the 1992/1993 season indicated that Sutherland was a competitive site when compared to other international observatory sites with the median seeing of $\sigma = 0.5''$. Later, extensive tests, summarized by Erasmus (2000), to determine the best site for the telescope included microthermal sensors deployed on a 30m mast, DIMM measurements from several locations, a SCIDAR scan of the atmospheric turbulence, and exhaustive meteorological tests. Results indicate the best seeing conditions occur with the Westerly wind, but the DIMM measurements indicate a median seeing of $FWHM = 0.92''$. The current height of the telescope should also be sufficient to escape the worse effects of the boundary layer (Erasmus 2000).

Current conditions at Sutherland Observatory have been continuously monitored by meteorological equipment and an active DIMM telescope. Recent analysis indicates that SALT is performing worse than the seeing measured by the DIMM; however at this moment, the degree of degradation caused by the telescope structure is poorly quantified due to an unknown source of degradation along the optical path.

3. Future Tests for AO Feasibility

We are currently planning a site survey at SALT in order to measure the feasibility of adaptive optical instrumentation. We plan to map the atmospheric C_n^2 profile through the following tests:

MASS/DIMMS: SAAO has acquired a MASS/DIMMS device from CTIO and plans to begin measurements in June 2007. MASS will provide measurement of the atmospheric conditions at 4-6 heights ranging from 0.5-16 km, while DIMMS will provide an integrated measurement of the atmosphere (Tokovinin et al. 2003).

Microthermal Sensors: Microthermal measurements for the site were made prior to the construction of SALT (Erasamus 2000), but no measurements have been made since then. Constructing the temperature gradient introduced by the dome structure will be important to limit the contributions of the structure to the image quality and a typical device would be expected to chart the atmospheric conditions within the 30m above the telescope structure.

Scintillation: By installing a speckle camera on SALT, simultaneous scintillation measurements from a single or double star can be made through analysis of the observed pattern from each of the 1m segments composing the primary mirror. Installation of temporary SCIDAR/SLODAR devices at the smaller telescopes at Sutherland will also provide measurements of the atmospheric conditions.

4. Adaptive Optics and the Future of SALT

Records of the atmospheric conditions combined with models of the atmospheric turbulence (Ellerbroek 2005) will provide a foundation for developing future AO projects. As SALT is primarily a spectroscopy telescope, even the introduction of a low order AO system will lead to significant improvement in the signal to noise and resolution for a fiber-fed spectrograph. Any traditional system for diffraction limited performance will require implementing the capability of phase deployment of the primary mirror, which was designed into the initial specifications (Buckley et al. 2005). However, the unique design of SALT with 91 independent mirrors allows for non-traditional systems. Exploration of these possibilities are left to the future, but include high speed imagers and interferometric systems.

The introduction of AO systems on SALT will provide significant gains in the telescope performance. As a queue based telescope, moderate increases in the median seeing allows greater flexibility in the scheduling and the selection of scientific programs. Furthermore, improvements in the best seeing open a new range of scientific questions that SALT could be used to address.

Acknowledgments.

SMC would like to thank the staff at SAAO and SALT especially David Buckley, Darragh O'Dooghue, and Fred Marang. SMC would also like to thank SAAO, the NRF, the NSF, and the meeting organizers for support to attend this meeting. Much of the early work on site testing for SALT was completed by Dr. D. A. Erasmus and it is with up most regret that he will not be able to continue this work along side us.

References

Buckley, D et al. 2005 IAU Sym. No 232

Ellerbroek, B. 2005, J. Opt. Soc. Am. A. 22, 310

Erasmus, D. 2000 SAJS 96

Gochermann J. et al. 1999, ExA, 9,1

Tokovinin, A. et al. 2003 MNRAS, 365, 1235

Climatology at the Roque de los Muchachos Observatory: tropospheric and ground level wind regimes

Antonia M. Varela* and Casiana Muñoz-Tuñón
Instituto de Astrofísica de Canarias, Tenerife, Spain

ABSTRACT

The Roque de los Muchachos Observatory (ORM) at La Palma (Canary Islands) is one of the two top sites preselected for hosting the future European Large Telescope (ELT), the other one is Paranal. Meteorological and seeing conditions are crucial for the site selection. Meteorological data provided by different ground Automatic Weather Stations (AWS) operating at the ORM from 1985 have been gathered and analysed in order to know the climatology and the local orographical effects. For analysis, day time and night time values have been separately considered. Here we also present the troposphere wind rose at the ORM –from climate diagnostic archives data- and the ground level wind roses and wind speed statistical results -from AWS ground data. We compare these results with those obtained at other astronomical observatories. At the ORM we have identified a high correlation between high and low altitude wind speed, which can be understood with the trade wind scenario favouring the astronomical observations and not significant climatic change.

---

*Corresponding author address:Antonia M. Varela, Instituto de Astrofísica de Canarias, C./Via Láctea, S/N, 38200-La Laguna, Tenerife, Canary Islands, Spain
E-mail: avp@iac.es

1. Introduction

General survey of sites requires the use of satellite data (cloud cover, precipitable water vapour, aerosol distribution, wind vertical profiles, etc.) and extensive meteorological and atmospheric turbulence databases in-situ studies to characterize site parameters to make a final selection.

Several site-testing campaigns have been performed at the Roque de los Muchachos Observatory at La Palma Island (see Figure 1), in particular, tests at the TNG and WHT sites (since 1992 to 1994) are presented in Muñoz-Tuñón et al. (1997) and the seeing and meteorological results of the campaign to select the site for the Gran Telescopio de Canarias (during 1995 and 1996) are summarized in Muñoz-Tuñón et al. (1997), Muñoz-Tuñón et al. (1998); Mahoney et al. (1998). From 1997 to 1999 a site testing campaign was continued at the GTC site till starting telescope construction in October 1999. In February 2002 we have started a campaign at the Hoyo Verde site, towards the SW of GTC site, near la Caldera. The proximity of this site to the Caldera necessitates continuous statistical meteorological tests over long period in order to ensure also a seasonal sample. The Caldera could also produce local fluctuations in the thickness of the surface layer.

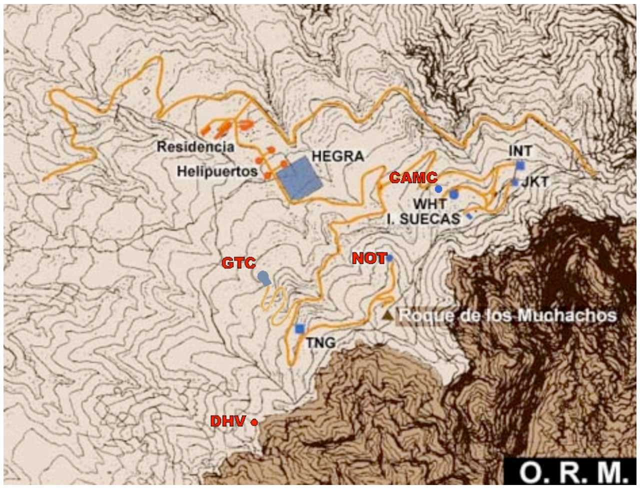

Fig.1 ORM map showing the different sites where the site-testing campaign was performed. These 4 stations can be representative of the entire ORM area.

Meteorological database has been recorded from several automatic weather stations (AWS) at the ORM indicated in table 1. In the table is also indicated the sampling rate, the total number of data and the period to which the measurements correspond. Occasional technical problems can modify the number of data of a particular parameter, then the number of data corresponds to the available wind data.

Table1. AWS meteorological database compiled for climatologic analysis. NOT corresponds to the AWS located at the Nordic Optical telescope, CAMC is the Carslberg Meridian Circle, GTC correspond to the data provide by the AWS at the Gran Telescopio de Canarias site, and the DHV is la Degollada del Hoyo Verde, towards the southwest of the GTC. Day and night time classification have been done by using solarimeter data monthly averages.

AWS	NDATA (day)	NDATA (night)	Period	Sample rate
NOT	415341	265496	feb'97-dec'03	1 data/5 min
CAMC	935838	606281	oct'85-jun'02	1 data/5 min
GTC	345624	300336	feb'95-dec'96	1 date/min
DHV or HV	443862	289552	feb'02-feb'04	1 data/min

The IAC weather stations (at the GTC and Hoyo Verde sites) have been provided by Casella Ltd. The Casella stations consist on a metal framework holding the data acquisition unit (DAU) and, at a height of 2m, a combined hygrometer and air temperature sensor, a solarimeter, a surface-wetness probe and a temperature-compensated barometer. A 12-m lattice tower supporting and anemometer and wind vane is erected near the station. The system is supplied with solar power generator and a radio communication system. The data logger can be programmed either to take instantaneous data or time averaged data. Thus the maximum instantaneous value during each minute period from 10s measurements is the gust value.

2. Statistical results

Meteorological data and statistics provided by the AWS are compiled by the Sky Quality Group of the IAC and are accessible at http://www.iac.es/project/sitesting/site.html. The information about the NOT and the CAMC weather stations are available from their corresponding project web pages (http://www.not.iac.es and http://www.ast.cam.ac.uk respectively).

Global statistical results for all meteorological parameters, daily and nocturnal time separately, provided by meteorological weather stations operating at the ORM are summarized in http://www.otri.iac.es/sitesting/index.php?flash=1&pag=9-61 and in Varela and Muñoz-Tuñón (2007).

2.1 Air temperature and relative humidity

Figures 2 show the diurnal and nocturnal mean and median air temperature (2m) and Figures 3 show values corresponding to mean and median relative humidity for the different AWS (see locations in Fig.1). There is a reciprocal relation between both

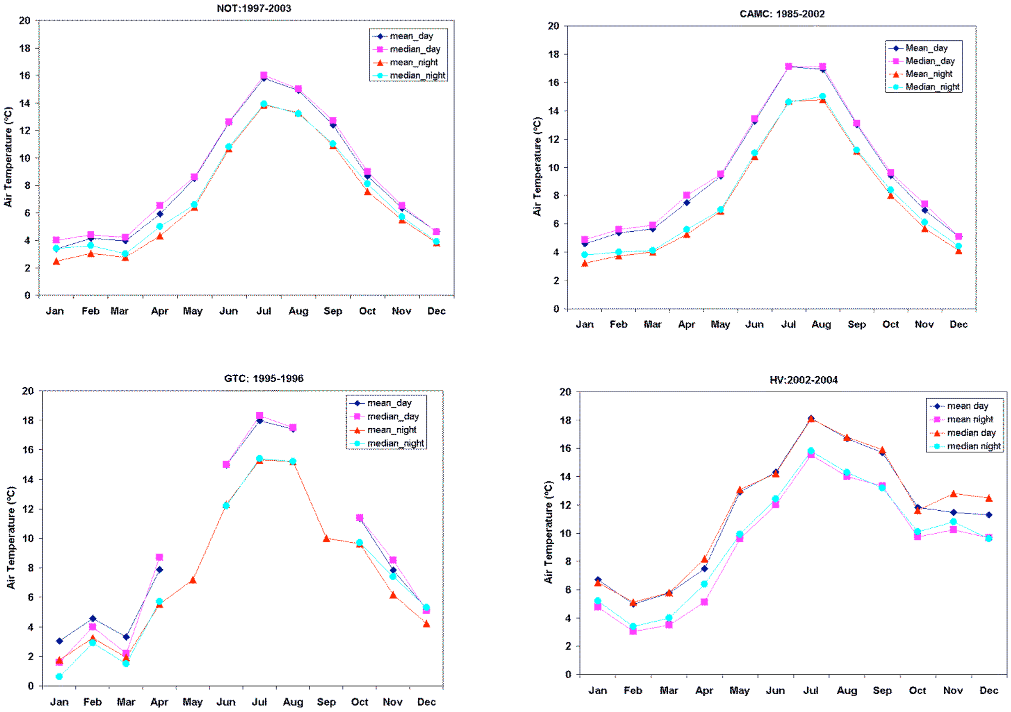

Fig. 2 Monthly mean an median air temperatures daytime and night time separately at different locations labelled in Fig.1.

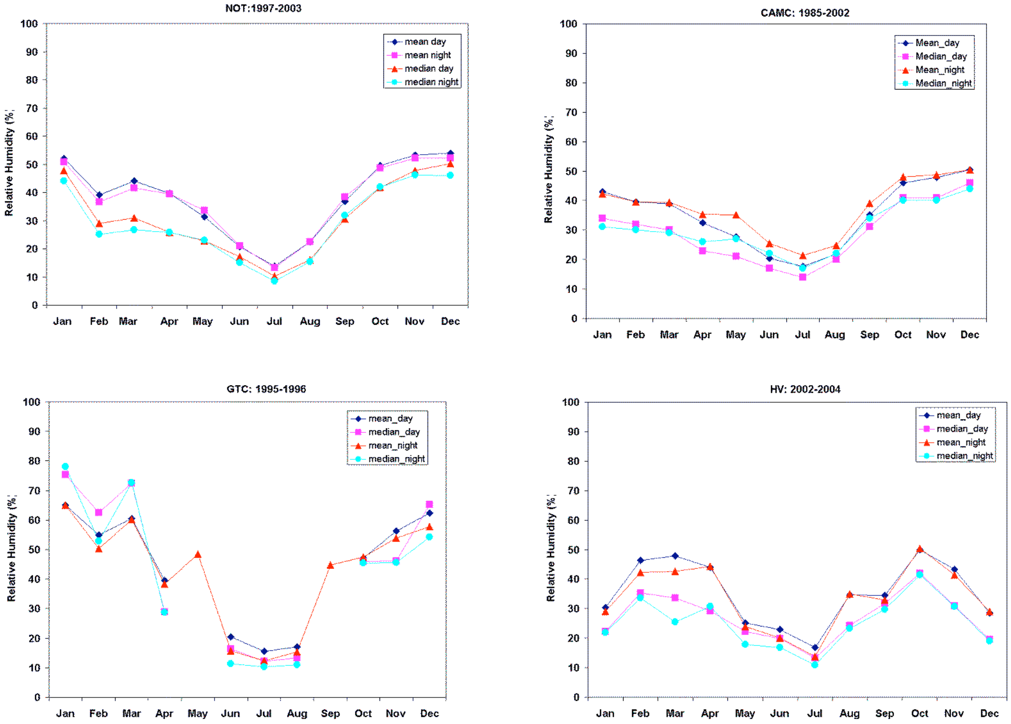

Fig. 3 Monthly mean and median relative humidity daytime and night time separately at different locations labelled in Fig.1.

parameters: the warmest summer months (June-September) are marked by extremely low relative humidity values (10% -35%) whereas the coldest winter months give the lowest mean monthly air temperatures and higher relative humidity (> 40%).

The difference in global mean air temperature between different locations can be explained in terms of difference in altitude and of the site soil properties. The air temperature profile does not indicate any climatic change tendency leading stable form this long period of time. The relative humidity shows yearly fluctuations trending to slightly smaller mean relative humidity from 1991 to 1998 when recovers and probably associated to local wind conditions.

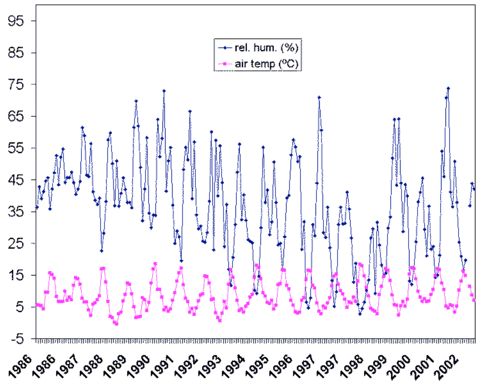

Fig. 4 Monthly air temperature and relative humidity recorded at the CAMC (the larger available database at the ORM) from 1986 till 2002.

2.2 Barometric Pressure

In Figures 5 we show the mean barometric pressure for the NOT, CAMC, GTC and HV sites respectively. Both day and night time measurements are quite similar, but there is a diurnal effect due to solar heating that increases the pressure difference by a mbar during clear days (more frequent in summer period). This effect is reduced to zero on days of cloud immersion.

The mean monthly daytime and night time barometric pressure follows closely similar patterns of behaviour throughout the years at every sites. There exists a seasonal dependence, the maximum mean pressure occurs in August (ranging from 783mbar at the GTC and 773mbar at the NOT), and the minimum in February and March. During the winter months (November/December and April/May), the occasional appearance of cold fronts introduces brief periods of considerable instability to the weather patterns and highest pressure dispersions.

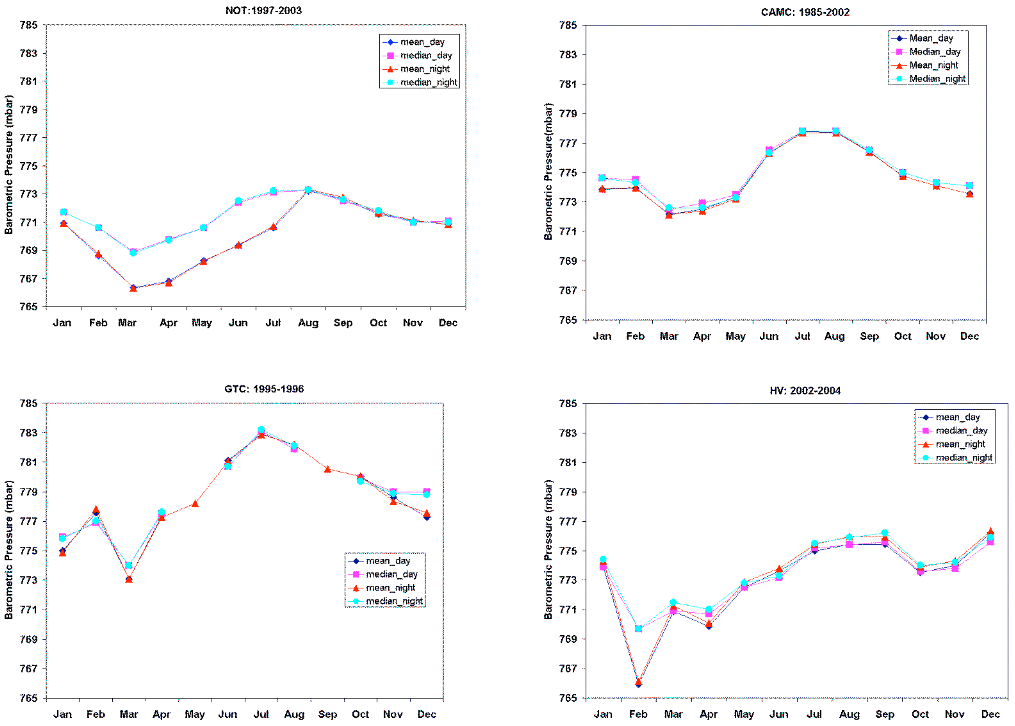

Fig. 5 Monthly mean an median barometric pressure daytime and night time separately at different locations labelled in Fig.1.

3. Troposphere and ground level wind speed and wind direction

Wind speed at 200mbar is one of the key parameters proposed for characterizing atmospheric turbulence above the Observatory (Sarazin and Tokovinin (2002), García-Lorenzo et al. (2005)). A lower average 200mbar wind speed is obtained at the ORM in comparison with other astronomical sites; furthermore, the ORM ranks first in suitability for adaptive optics suitability (García-Lorenzo et al. (2005)). The usefulness of this value might be conditional on the continuity of the wind value and wind direction from the upper troposphere to the ground level. With this motivation we are undertaking a study of tropospheric and ground winds at several observing sites.

In this contribution we analyse the wind speed and wind direction statistics, for day and night time separately, obtained from data recorded at different sites at the ORM with several automatic weather stations installed since 1985. Wind speed and wind direction are compared with those obtained from 200mbar to 700mbar climate diagnostic archives data. The existing correlation between high and low altitude wind speed can be understood in terms of the trade wind scenario.

3.1 Ground level wind speed and wind direction at the ORM

The stability of ground wind speed distribution, wind direction and gradients, and the maximum tolerable wind affect telescope and dome designs as well as contributing to the image quality degradation. Images of the stars in high wind velocity conditions are sometimes blurred even by the shaking caused by the wind.

Table 2. Statistical wind speed results at different locations in the ORM (day and night given separately). The mean and median values recorded at the NOT, GTC and DHV sites are coincident in the range 5-6m/s and for the expected value when we extrapolate from the 700mbar wind speed – see next section - but not for those recorded at the CAMC location. The mean wind speed at the CAMC from data gathered between 1987 and 1995 is 2m/s (Jabiri et al. (2000)); an identical result is shown in this paper using the 1984-2003 database and reveals lower values corresponding to a unevenly location, unexpected for summits of the island and unrepresentative of the wind behaviour at the entire Observatory.

AWS	NOT day	NOT night	CAMC day	CAMC night	GTC day	GTC night	DHV day	DHV night
Mean (m/s)	6.06	6.91	2.33	2.48	5.54	5.78	5.33	5.55
Std (m/s)	3.88	4.14	1.90	1.99	3.27	3.39	2.83	3.00
Median(m/s)	5.40	6.40	2.00	2.00	4.78	5.25	5.10	5.45
Max(m/s)	34.90	37.50	20.00	23.00	29.52	41.28	25.35	26.78

The yearly average ground wind speed at Paranal (750mbar) is 6.6m/s (http://www.eso.org//paranal/site/paranal.html) and the median wind speed at Mauna Kea (615mbar) is 7m/s, Sarazin (2003). In the foothills of a major mountain chain such as Maidanak the ground mean velocity is 3m/s, Ehgamberdiev et al. (2000).

Figure 6 presents the ground level daytime and nocturnal wind roses at different locations at the ORM, i.e. NOT, DHV, GTC and CAMC. Orographical components appear at ground level determining a marked change in the day wind-vector pattern. The effect is obviously related to heat from the Sun and the results in a up draught causing diurnal winds normal to the orographical contours and differences of about a 10% of the mean wind speed in nocturnal and daily wind speed.

Figure 7 shows the cumulative frequency of wind speed and wind gust at different locations in the ORM. If 15m/s would be the practical limit of operation, the useful observing time ranges from 92-99%.

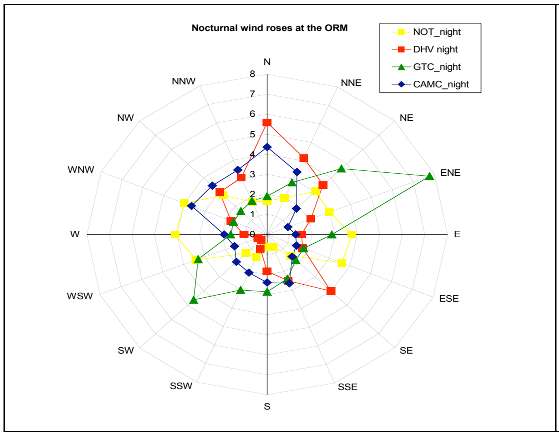

Fig. 6 Ground level daytime and nocturnal wind roses at different locations at the ORM, i.e. NOT, DHV, GTC and CAMC.

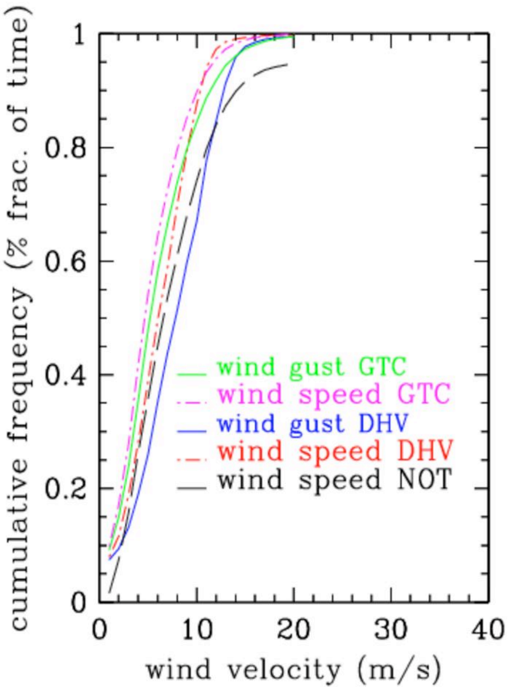

Fig. 7 Cumulative frequency of wind speed and wind gust at different locations in the ORM.

3.2 Tropospheric wind regimes: from 200mbar to 700mbar

Tropospheric winds at several astronomical observatories for the period 1980-2002 have been selected from the climate diagnostic model and the balloon NCEP/NCAR databases. Ground level winds are provided by local automatic weather stations. Figure 8 shows the monthly mean wind speed at Roque de los Muchachos Observatory for different pressure levels: 200mbar - 12169.9m above sea level, 300mbar (9598.51masl), 400mbar (7574.75masl), 500mbar (5808.73masl), 600mbar (4390.95masl) and 700mbar (3151.02masl) and for ground level (~775mbar), day and night separately. Results at other observing sites are presented in García-Lorenzo et al. (2005).

The mean and median wind speed decrease continuously with height, ranging from 22.5 m/s at 200mbar to 8.6m/s at 700mbar (day + night). If we extrapolate to wind speed values at 775mbar (mean height where ground automatic meteorological stations are installed), we would typically expect 5-6m/s velocity values, which is coincident with the values provided by ground level automatic weather stations.

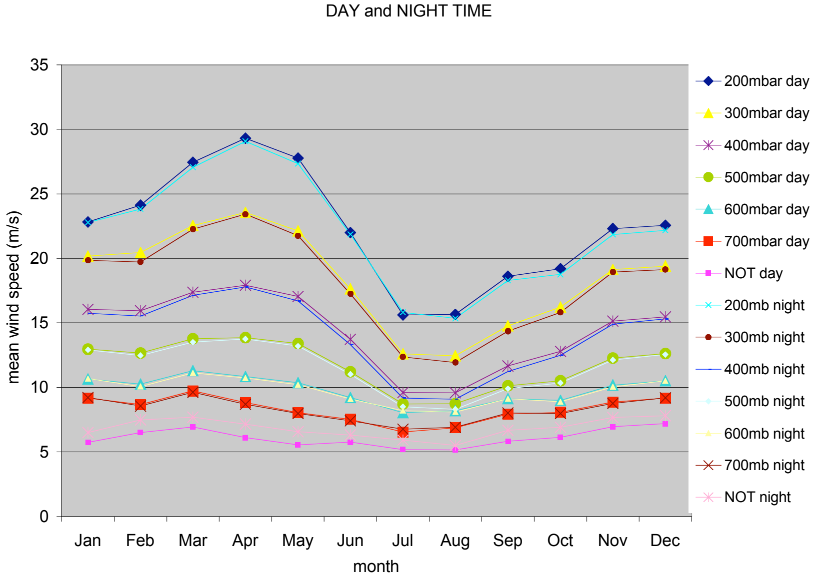

Fig. 8 Monthly wind profiles at the ORM from 200mbar to ground level (NOT is at 775 mbar).

In order to show the connection of high to low altitude winds as a first approach to this relationship at the studied sites, we have compared the six-hourly and daily wind speed measurements at the different pressure levels (except 700mbar for Mauna Kea, that is always below the site altitude) with the simultaneous wind data at 200mbar. In Figure 9 (from García-Lorenzo et al. (2004)) the Pearson correlation coefficients are shown. Winds at the lowest levels, 700mbar or 600mbar for Mauna Kea, could be affected by the topography of the sites, and may be breaking the linear relationship.

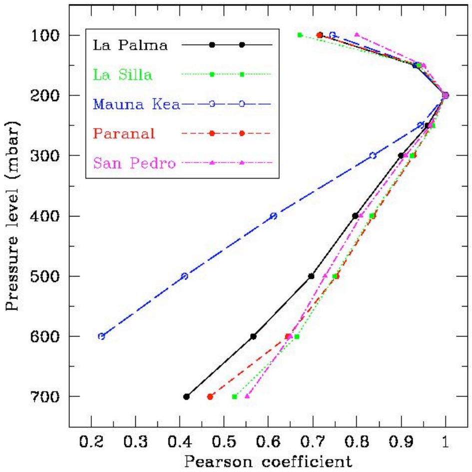

Fig. 9 Pearson correlation coefficients form any pressure level at different astronomical observatories (indicated on the plot). García-Lorenzo et al. (2005).

The high to low altitude wind correlation coefficients follow a similar behavior at all the sites except for Mauna Kea. This similar behavior could suggest a similar relationship to that found at Paranal for La Palma, La Silla and San Pedro Mártir. Nevertheless, the lack of correlation between the 200mbar and the low level wind speeds in Mauna Kea can be interpreted in terms of the wind vertical propagation and of the local topography that can introduce shear effects. The propagation of this wind flux in height and its correlation with ground level winds is crucial to understand their influence on image quality.

To understand the tropospheric wind correlation at different observing sites we have analysed the wind roses or relative frequency of a determined wind direction (day and night time together) at different pressure levels from 200mbar to 700mbar, calculated from the data provided by the NCEP/NCAR (Varela et al. (2006); Varela and Muñoz-Tuñón (2007)).

Tropospheric wind roses at Paranal and La Silla are similar. The anticyclonic circulation (W-WNW) is the dominant component at all pressure levels and shifts slightly to the north-west at low level (peaking NW at Paranal at 700mbar and WNW at La Silla at 700 mbar). In San Pedro Mártir the wind rose follows the trade wind pattern close to those obtained at the ORM but peaking to the south and south-east at the lower levels Nevertheless, at Mauna Kea the wind direction peaks to the west from 200 to 500mbar and dramatically shifts ENE-E at 600 and 700mbar – also becoming more intense in velocity. This abrupt change in direction can explain the lack of correlation between the 200mbar and the ground level wind speeds and can also play an important role in low level atmospheric turbulence as a consequence of wind shear. In this case the 200mbar wind speed would be insufficient to estimate the atmospheric turbulence, and in situ measurement would be necessary (Varela et al. (2006)).

4. Conclusions

1. An important factor for determining the stability of observing conditions is the air temperature gradient along the night, which typically ranges between 2 and 4ºC. The typical difference between the day and night time mean air temperature is about 2ºC at any location at the ORM.

2. Wind speed statistical results from data recorded at different automatic weather stations operating at the ORM provide typical mean and median wind speeds at the ORM ranging from 5 to 6m/s, except at the CAMC (due to its particularly leeward location).

3. If 15m/s would be the practical limit of operation, the useful observing time ranges from 92 to 99%.

4. The propagation of the wind flux in height and its correlation with ground level winds are crucial to understanding the influence of the trade winds on image quality. The high to low altitude wind correlation coefficients follow a similar behaviour at the sites studied except for Mauna Kea. This similar behaviour could suggest a similar relationship as that found at Paranal for La Palma, La Silla and San Pedro Mártir. Mauna Kea shows smaller Pearson correlation coefficients suggesting a weaker connection of high and low altitude winds. Winds at the lowest levels, 700mbar or 600mbar for Mauna Kea, could be affected by the topography of the sites, perhaps breaking the linear relationship.

5. High altitude winds can be a useful parameter for astronomical site evaluation when correlated with the surface layer winds.

Acknowledgments.

This work has been carried out under the framework of the European Project OPTICON as part of its specific objectives and under the FP6 Proposal for Site Selection for the European ELT. For this study we have made use the NCEP Reanalysis data provided by NOAA-CIRES Climate Diagnostic Center, Boulder, Colorado, USA, from their web site at http://www.cdc.noaa.gov/. We give our thanks to the CAMC and NOT groups for providing AWS meteorological database from their web pages: http://www.not.iac.es/cgi-bin/weather-archive.pl and http://www.ast.cam.ac.uk/~dwe/SRF/camc_met_records.html.

References

Ehgamberdiev S.A, A.K. Baijumanov, S.P. Ilyasov, M. Sarazin, Y.A. Tillayev, A.A. Tokovinin and A. Ziad, 2000: Astron.Astrophys.Suppl.Ser. 145, 293.

García-Lorenzo B., J.J. Fuensalida, C. Muñoz-Tuñón and E. Mendizábal, 2005: MNRAS, 356, 849

Jabiri A., Z. Benkhaldoun, J. Vernin and C. Muñoz-Tuñón, 2000: A&A Suppl.Ser. 147, 271.

Mahoney, T., C. Muñoz-Tuñón and A.M. Varela, 1998: New Reviews in Astronomy, Eds. C. Muñoz-Tuñón, 417.

Muñoz-Tuñón, C., J. Vernin, J. and A.M. Varela, 1997: A&A, 125, 183.

Muñoz-Tuñón, C., A.M. Varela and T. Mahoney, 1997: Campaña de Prospección Astronómica del Lugar Idóneo para la Instalación del Telescopio de 10m, Informe Final.

Muñoz-Tuñón, C., A.M. Varela and T. Mahoney, 1998: New Reviews in Astronomy, Eds. C. Muñoz-Tuñón, 409.

Sarazin M. And A. Tokovinin, 2002: in Vernet A.E., Ragazzoni R., Esposito S. & Hubin, N. eds. , proc. 58th ESO Conference Workshop, Beyond Conventional Adaptive Optics, ESO Publication, Garching, p.321.

Sarazin M., 2003: ESPAS Site Summary Series : Mauna Kea, Issue 1.2

Varela, A.M., C. Muñoz-Tuñón, B. García Lorenzo and J.J. Fuensalida, 2006: Proc. Of SPIE Vol. 6267, 62671X-1.

Varela, A.M. and C. Muñoz-Tuñón, 2007: MNRAS (in preparation)

Preliminary study of the seasonal variation of optical seeing above Oukaïmeden site in the Moroccan High Atlas Mountains

Abdelouahed Abahamid*, Benkhaldoun Zouhair and Youssef El Azhari
Laboratoire de Physique des Hautes Energies et Astrophysique
Cadi Ayyad University, Marrakech

ABSTRACT

The first seasonal variation study extended over fifteen months of the night time seeing above the Oukaïmeden site is reviewed. These data was measured in the visible during 137 nights distributed along the period July 2003 - September 2004 with the Differential Image Motion Monitor of Marrakech (DIMMAR) on top of a 5 meters high tower. From the whole campaign the mean seeing is 0.92", the median value is 0.84" and the best seeing measured is 0.32". We determinate that the best season is summer, its seeing median value is 0.78". The best monthly median seeing, 0.60", is observed in september.

**Corresponding author address:* Abdelouahed Abahamid, LPHEA, Cadi Ayyad University, Marrakech
E-mail: a.abahamid@ucam.ac.ma

Analysis of diurnal and seasonal variation of Fried's coherence length, isoplanatic angle, and greenwood frequency

Darielle Dexheimer* and Marjorie Shoemake
Boeing LTS

ABSTRACT

PAODMS seeing data were collected at the SOR from August 1998 through October 2002. Weather permitting, the data were collected 24/7, to characterize the diurnal statistics of Fried's coherence length, r_0, the isoplanatic angle, θ_o, and the greenwood frequency, f_g. Since October 2002, data have been collected as required to support experiments conducted at the SOR. These data are predominately night data. This report documents preliminary results of the distributions of the seeing parameters. The output data format changed in May 2000, so this report covers only the period May 2000 – January 2004.

**Corresponding author address:* Darielle Dexheimer, Boeing LTS.
E-mail: darielle.dexheimer@kirtland.af.mil

Atmospheric conditions by dust pollution over ELT sites

El Arbi Siher* and Benkhaldoun Zouhair
Laboratoire de Physique des Hautes Energies et Astrophysique
Cadi Ayyad University, Marrakech

ABSTRACT

In a previous studies (Siher et al. 2004, 2006a and 2006b), we showed that the astronomical observation (atmospheric extinction) is affected by the Saharan and Sahel dust. In this paper, we will use the TOMS/EP aerosol index to show how are the ELT sites influenced by this pollution. This study will present some maps of this pollution.

**Corresponding author address:* El Arbi Siher, LPHEA, Cadi Ayyad University, Marrakech
E-mail: siher@fstbm.ac.ma

How to Monte-Carlo Simulate the Optical Turbulence Boiling beyond the Frozen Flow Hypothesis

Amokrane Berdja* and Julien Borgnino
LUAN–UMR 6525, Université de Nice-Sophia Antipolis

ABSTRACT

High Angular Resolution through turbulence requires an accurate description of the optical turbulence time-variations. As for spatial fluctuations, time-variations of the optical turbulence observables are random. Their statistical and spectral properties are however reproducible. This property allows performing Monte-Carlo simulations of the spatial distributions and time-variations of the optical turbulence observables such as phase fluctuations or scintillation. The optical turbulence time-variation is usually described by the so-called Frozen Flow Hypothesis in which turbulence is supposed to be equivalent to a series of solid phase-screens that slide horizontally across the observation field-of-view. Experimental evidence shows however that an additional physical process must be taken into account. In fact, while translating above the observer, turbulence undergoes a proper time-variation which affects differently the astronomical observations. The proper time-variation of the optical turbulence observables as described here will be called the optical turbulence boiling in the following. The central topic of our discussion concerns the optical turbulence time-variation beyond the paradigm of the frozen flow hypothesis, and how to Monte-Carlo simulate the optical turbulence boiling effect. The usual simulation consists in generating a two-dimensional spatially distributed phase-screen and to move it schematically over the telescope entrance aperture. The spatiotemporal statistical properties depend upon the spatial power spectrum of the phase-screen and upon the wind velocity. In our approach to model the optical turbulence boiling, we will first discuss how to establish a spectral description of the boiling process. This description leads formally to a redistribution of the optical turbulence energy over time-frequencies. It also make it possible to Monte-Carlo simulate the time-variation of an optical turbulence spatial distribution such as phase fluctuations at the entrance pupil of telescope through the optical turbulence boiling process. The spatiotemporal statistical properties depend then upon the spatial power density of the optical turbulence observable and upon a boiling constant we introduce while discussing the theoretical approach. We present then a Monte-Carlo simulation method of a time-varying spatial distribution of phase fluctuations through the optical turbulence boiling, which is based upon variation of the usual FFT-based method for phase-screen generation. This method can be easily generalized to the case in which both the optical turbulence boiling and horizontal transportation by the wind are involved in a multilayered-turbulence configuration. In this case the boiling optical turbulence must be moved over the telescope so that the spatiotemporal statistical properties of the time-varying observable depend upon the spatial spectral densities, boiling constants and wind velocities across the turbulence vertical profile above the telescope

---

**Corresponding author address:* Amokrane Berdja, LUAN–UMR 6525, Université de Nice-Sophia Antipolis.
E-mail: berdja@unice.fr

El Roque de Los Muchachos Site Characteristics

G. Lombardi[1,2,3], V. Zitelli[2], S. Ortolani[4], M. Pedani[5]

1. Department of Astronomy, University of Bologna, Bologna (Italy)
2. INAF – Bologna Astronomical Observatory, Bologna (Italy)
3. ESO – European Southern Observatory, Santiago (Chile)
4. Department of Astronomy, University of Padova, Padova (Italy)
5. Fundación Galileo Galilei and Telescopio Nazionale Galileo, Tenerife (Spain)

Send offprint request to: gianluca.lombardi@oabo.inaf.it

1. Introduction

The Observatorio del Roque de Los Muchachos (ORM) is located at La Palma Island (Canaries). The very good astronomical conditions of the island are mainly due to a stable subsiding maritime air mass.

All the telescopes are located well above the inversion layer occurring in the range between 800 and 1200 m, along the northern edge of the Caldera de Taburiente, at the northwest side of La Palma where the irregular shapes produce a complex orography, and the crowdedness of the top, due to the presence of all the astronomical observatories, suggests the local microclimate to differ from site to site and making it difficult to foresee in advance the precise local meteorological parameters.

We present an analysis of the mean meteo parameters taken at Telescopio Nazionale Galileo (TNG), Carlsberg Automatic Meridian Circle (CAMC) and Nordic Optical Telescope (NOT). Analyses of data from the TNG, CAMC and NOT are compared in order to check local microclimate variations and long-term trends. Table 1 reports the positions and the altitudes above sea level of the three telescopes.

TABLE 1. Positions and altitudes of TNG, CAMC, and NOT.

	LATITUDE	LONGITUDE	ALTITUDE A.S.L. [M]
TNG	28°45’28.3’’ north	17°53’37.9’’ west	2387 (Elevation Axis)
CAMC	28°45’36.0’’ north	17°52’57.0’’ west	2326 (Dome floor)
NOT	28°45’26.2’’ north	17°53’06.3’’ west	2382 (Dome floor)

2. Data description

Meteorological data are obtained from TNG, CAMC, and NOT weather stations located in places not influenced by the presence of the domes. The three telescopes are lies on an imaginary straight line in NE direction: TNG and CAMC are about 1000 m far, while NOT is placed in the middle at about 500 m from TNG.

The database of TNG is 7 yr long (1998-2005), NOT is 8 yr long (1997-2005), while CAMC is 20 yr long (1985-2004). We analyzed temperature (*T*), wind speed (*wsp*), relative humidity (*RH*), and air pressure (*P*). From each raw data series, we compute the hourly averages, and then from each set of these, we compute the monthly averages and finally the annual averages. Vectorial wind direction is evaluated by calculating the annual percentage of hours in which the wind comes from fixed directions.

3. Microclimate differences between the three sites

The CAMC 20 yr annual temperatures baseline (Figure 1) shows an increasing trend (about 1.0 deg per 10 yr). Is this the first confirmation of global warming above the inversion layer?

CAMC and TNG trends are remarkably similar, with average temperatures differing by no more than 0.6 deg (Lombardi et al. 2006). CAMC is the driest site, maintaining a $RH < 58\%$ in wintertime (Figure 2, top) and $RH < 44\%$ in summertime (Figure 2, bottom), while both

TNG and NOT have comparable trends and appear to dampen 15% on average in wintertime and 7% in summertime (Lombardi et al. 2007).

CAMC has the highest pressures (773-776 hPa). Figure 3 shows an increasing behaviour through 20 yr. Does it drive temperature increasing? NOT shows lower pressures (771-772 hPa). TNG display big differences compared to NOT in 2000 and 2002, but very similar values in 2003, 2004, and 2005. The barometric correction applied to P for the three sites demonstrates that ORM is dominated by high pressure (Lombardi et al. 2007).

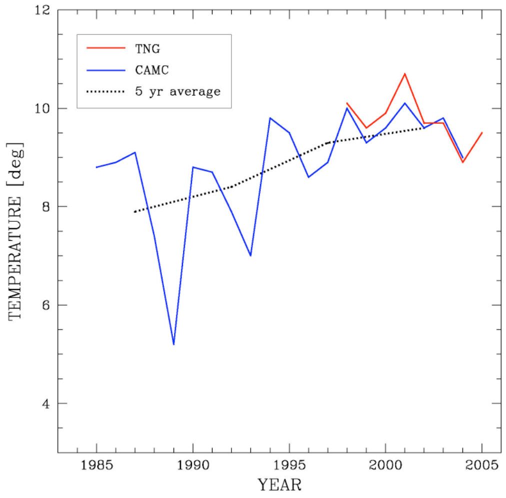

FIGURE 1. Annual temperatures.

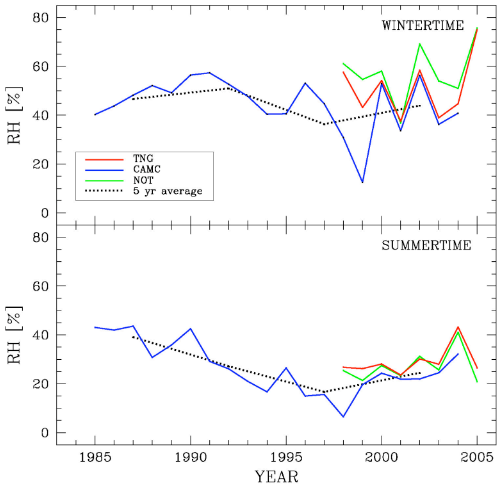

FIGURE 2. Annual relative humidity.

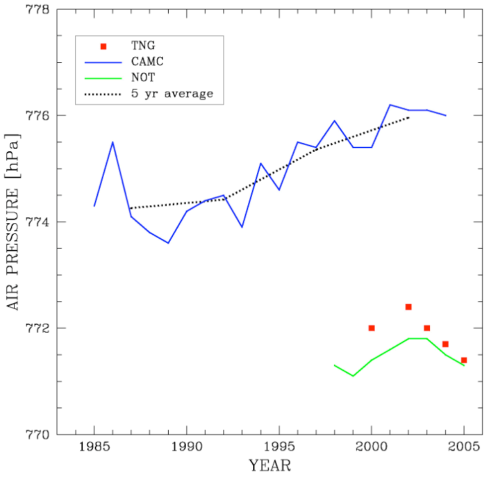

FIGURE 3. Annual air pressure.

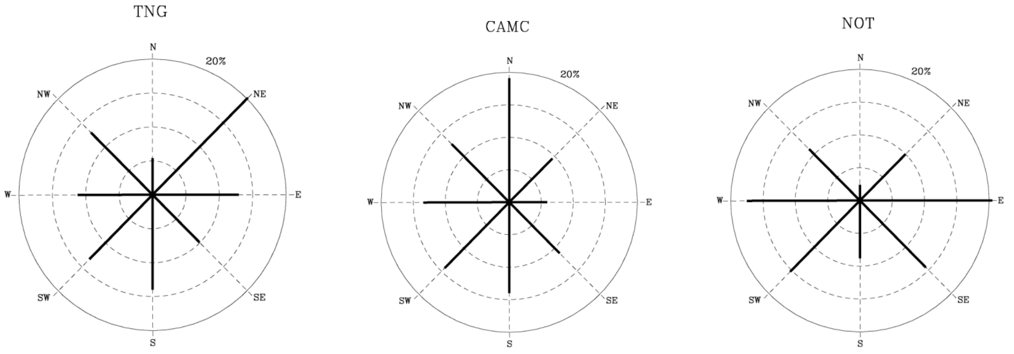

FIGURE 4. Nighttime windroses for TNG, CAMC and NOT in the common period 1998-2004 (Lombardi et al. 2007).

TABLE 2. Nighttime wind speed statistics.

WIND SPEED [M S^{-1}]	TNG [%]	CAMC [%]	NOT [%]
wsp < 3.3	30.2	83.6	18.5
$3.3 \leq wsp < 12$	68.4	16.4	70.2
$12 \leq wsp < 15$	1.1	0.0	7.1
$wsp \geq 15$	0.3	0.0	4.2

The three telescopes show different dominant wind directions both in daytime and in nighttime demonstrating that the typical wind direction significantly changes across the site. Figure 4 shows the nighttime windroses in the three sites calculated as percentage of hours in which the wind comes from fixed directions.

Table 2 shows the percentage of time computed for four values of wind speed (Lombardi et al. 2007). TNG and NOT have optimal observing conditions ($3.3 \leq wsp < 12$ m s^{-1}, see Section 4 and Figure 6) about 70% of the time, compared to 16.4% at CAMC. The evaluation of time in which $wsp \geq 15$ m s^{-1} gives an estimation of the downtime due to high wind velocity. The lost time at TNG is only 0.3% of the total. CAMC never shows $wsp \geq 12$ m s^{-1}, and NOT is more affected by high wind speed (4.2%).

4. Temperature, wind speed and astronomical seeing

We use 118 images obtained with the Optical Imager of Galileo at TNG in *V* band, pointed near the zenith (and corrected to true zenith by a small amount) from 2000 January 31 to February 4.

The image quality in terms of FWHM is compared to the difference in temperature (*DT*) between the ground temperature and the temperature at the level of the TNG primary mirror:

$$DT = T(G) - T(M1)$$

Figure 5 shows that seeing deteriorates when $DT > -0.6$ deg. This can be explained as a consequence of the higher temperature at the level of the primary mirror that inhibits the thermal convection below (Lombardi et al. 2006).

The FWHM are also compared to the wind speed (Figure 6). We see that 50% of the points are distributed below a wind speed of 3.3 m s^{-1} (red dashed line), with median FWHM of 1.5 arcsec. For $wsp \geq 3.3$ m s^{-1}, the distribution of the points has a median value of 1.3 arcsec. This indicates that we have optimal observing conditions when $wsp < 3.3$ m s^{-1} (Lombardi et al. 2007).

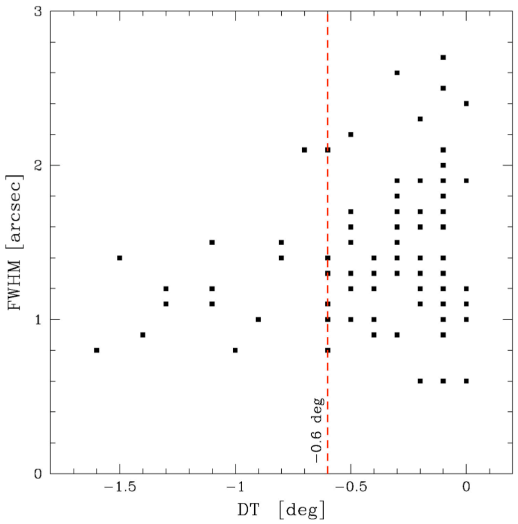

FIGURE 5. Seeing in *V* band vs *DT*.

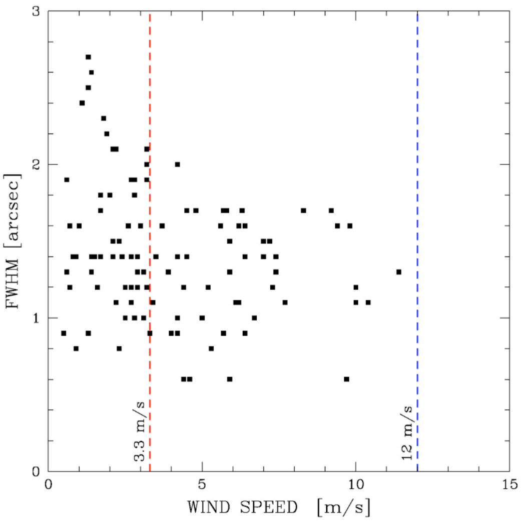

FIGURE 6. Seeing in *V* band vs wind speed.

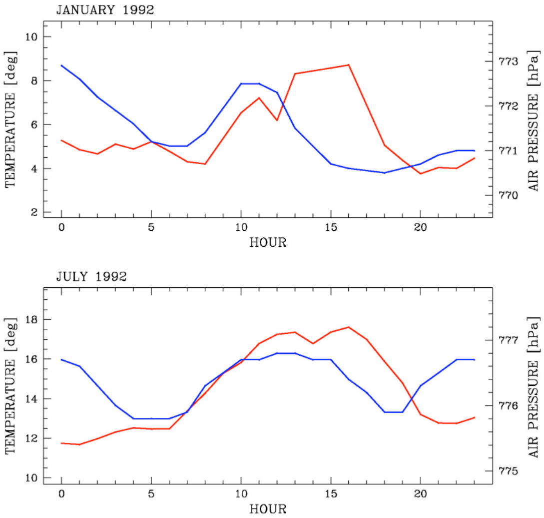

FIGURE 7. Hour-to-hour pressure (blue) and temperature (red) trends at CAMC in 1992.

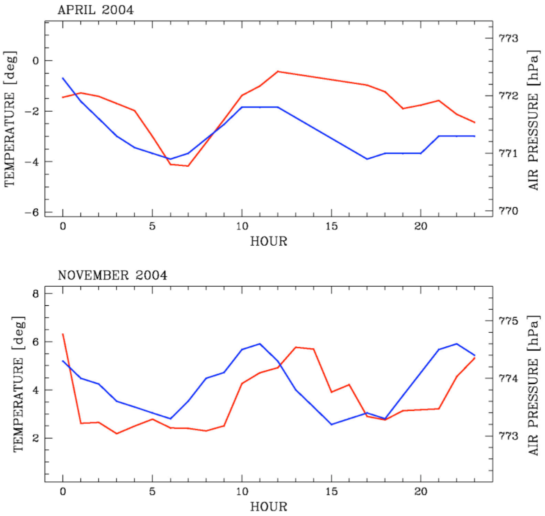

FIGURE 8. Hour-to-hour pressure (blue) and temperature (red) trends at CAMC in 2004.

5. Short-time scale thermalization forecasting

Figure 7 and Figure 8 show that pressure changes anticipate changes in temperature, typically by 2–3 hr, in both the wintertime and summertime (years 1992 and 2004 are taken as examples).

The relationship between *P* and *T* suggests the following question: is it possible to foresee the changes in temperature a few hours in advance, on the basis of the changes in air pressure?

If YES, it could be possible to optimize the thermalization of the telescope and the instruments, reducing the instrumental seeing.

The correlation between air pressure and the temperature measured 2 hr later has a confidence level 98%. This correlation typically decreases if temperatures are measured 1 hr (c.l. 84%) or 3 hr (c.l. 95%) later. The ability to make predictions based on hour-to-hour analyses vanishes on timescales higher than a few hours (Lombardi et al. 2007).

Acknowledgements. The authors acknowledge the CAMC and NOT staff for making the meteorological data available online. G. Lombardi also thanks Ernesto Oliva of TNG for the useful information and data; Jose L. Muiños Haro of CAMC for his kindness, support with the data, and information; Ricardo Javier Cárdenas Medinas and Peter Meldgaard Sorensen of NOT for their help and patience; and A. Bragaglia for the useful images from TNG.

References

Lombardi G., Zitelli V., Ortolani S., and Pedani M., 2006, PASP, 118, 1198
Lombardi G., Zitelli V., Ortolani S., and Pedani M., 2007, PASP, 119, 292

FIRST AUTHOR INDEX